

Classification of Atrial Ectopic Beats into Spatial Segments based on the 12-lead ECG

Master Thesis

submitted by

B.Sc. Pedro Álvarez Guirado



Institute of Biomedical Engineering
Prof. Dr. rer. nat. Olaf Dössel
Prof. Dr. rer. nat. Werner Nahm
Karlsruhe Institute of Technology
2018

Supervisor: M.Sc. Steffen Schuler

Statutory declaration

I declare that I have authored this thesis independently, that I have not used other than the declared sources/resources, and that I have explicitly marked all material which has been quoted either literally or by content from the used sources.

Karlsruhe, September 9, 2018

Abbreviations

AFib	atrial fibrillation
BSPMs	body surface potential maps
CTI	cavotricuspid isthmus
CV	conduction velocity
ECG	electrocardiogram
LA	left atrium
LAA	left atrial appendage
LIPV	left inferior pulmonary vein
LV	left ventricle
MLP	multilayer perceptron
NN	neural network
PCA	principal component analysis
RA	right atrium
RAA	right atrial appendage
RSPV	right inferior pulmonary vein
RV	right ventricle
SA	sino-atrial node

Abstract

Atrial tachyarrhythmias such as atrial fibrillation (AFib) predispose to ventricular arrhythmias, sudden cardiac death and stroke. The complex and rapid atrial electrical activity makes it difficult to obtain detailed information on atrial activation during fibrillatory conditions. However, ectopic foci are often involved in initiating and sustaining AFib and therefore identifying the origin of atrial ectopic activity can help in diagnosis and treatment of AFib. Currently, invasive catheter mapping and ablation remains the cornerstone for the treatment of atrial arrhythmias. Non-invasive tools to guide electrophysiologists could significantly shorten catheter mapping procedures and may ultimately decrease the recurrence rate of ablations. Existing approaches are based on the analysis of the main characteristics of body surface potential maps (BSPMs), such as the P-wave polarity, or rely on inverse reconstructions of the electric activity of the heart from BSPMs (ECG imaging). However, these methods have not yet shown to be accurate and reliable enough to be implemented in standard clinical practice. As the 12-lead electrocardiogram (ECG) is already routinely recorded in clinical settings, its use for classification of atrial ectopic foci into spatially differentiated atrial segments has been explored in this thesis. Atrial segments were defined with an automatic geodesic algorithm and a neural network (NN) was used for classification. Our simulation results with 8 atria-torso models show that ectopic foci with similar 12-lead ECG naturally cluster into differentiated atrial regions and that new patterns could correctly be classified into 29 segments with an accuracy of approximately 85%. Results also suggest that it is possible to predict whether the ECG signal belongs to the left atrium (LA) or the right atrium (RA) with an accuracy of 95%. If the classifier is applied to a new geometry that has not been used for training, however, the classification accuracy decreases drastically.

Acknowledgments

It is important to acknowledge the giants whose shoulders we stand upon. I would, therefore, like to thank the many who offered advice and help along the way, including my supervisor Steffen Schuler, without your help this thesis could not be possible. Also, I would like to thank KIT and in particular IBT for accepting me as one of them.

To my parents, this is for them, for teaching me that "It is not how many times you fall that matters, it is how many times you get up."

Contents

Abbreviations	i
Abstract	iii
Acknowledgments	v
1 Introduction	1
1.1 Motivation and Objective	1
1.2 Goal of this Research	2
1.3 Outline	2
<hr/>	
I Fundamentals	5
<hr/>	
2 Medical Fundamentals	7
2.1 Cardiac Anatomy	7
2.2 Cardiac Physiology	8
2.3 The Physical Basis of Electrocardiography	8
3 Mathematical Fundamentals	13
3.1 The Fast Marching Method	13
3.2 Geodesic	14
3.3 Principal Component Analysis	14
3.4 FastICA	15
3.5 Supervised Learning Methods for Classification / Neural Networks	15
<hr/>	
II Methods	19
<hr/>	
4 Materials	21
4.1 Atria models	22

4.2	Torso models	22
5	Methods	25
5.1	Left and Right atrium separation	25
5.2	Atria segmentation	28
5.3	Excitation simulations	40
5.4	Torso forward calculations	41
5.5	Feature extraction	43
5.6	Classification	46
<hr/>		
III	Results	53
<hr/>		
6	Atria segmentation results	55
6.1	Left atrium segmentation results	55
6.2	Right atrium segmentation results	56
7	Classification results	59
7.1	LA and RA classification	60
7.2	Random data division	61
7.3	Atria data division	65
7.4	Torso data division	66
8	Conclusion	71
8.1	Geometrical aspects	71
8.2	Classification aspects	72
9	Outlook	73
<hr/>		
IV	Appendix	75
<hr/>		
10	Results for area-aligned ECG signals	77
	List of Figures	81
	List of Tables	87
	References	89

Introduction

1.1 Motivation and Objective

The non-invasive localization of atrial ectopic foci during focal atrial tachycardia is complex to determine. Methods based on either standard 12-lead ECG or body surface potential maps BSPMs have not shed sufficient light on how to accurately correlate ectopic focus locations with the distribution of potential and P-wave characteristics on the torso surface. This limitation results in longer intra-operative invasive mapping procedures, which could lead to suboptimal localization and ablation of focal triggers. [1]

From the early 70's, several approaches have been proposed to localize ectopic foci in the atria. The first studies in humans consisted in pacing the atria at different sites to analyse the morphology, time sequence and polarity of P-waves using the standard 12-lead ECG. [2]

Unfortunately, the usability of standard 12-lead ECG for such analysis is limited due to the number of P-waves with low amplitude or isoelectric morphology. In the late 90's, some studies increased the number of body surface electrodes and focused on studying the body surface potential distribution or the body surface integral P-wave maps during controlled atrial pacing. [3]

More recently, a combination of BSPM with surface wavefront propagation maps have been proposed. [4] However, none of those approaches based on the forward problem have provided an efficient and reliable method to localize the specific origin of the ectopic excitation.

Recent studies have focused on designing and validating algorithms based on P-wave polarity that used 12-lead or 64-lead recordings for identifying the origin of ectopic sites. Those procedures show a general good accuracy for detecting the site of some ectopic foci. However, their accuracy decreases again when bi-phasic P-waves are present in many leads. [5]

Further methods propose to build a database of simulated BSPM combined with machine learning techniques to predict the localization of ventricular ectopic triggers. [6]

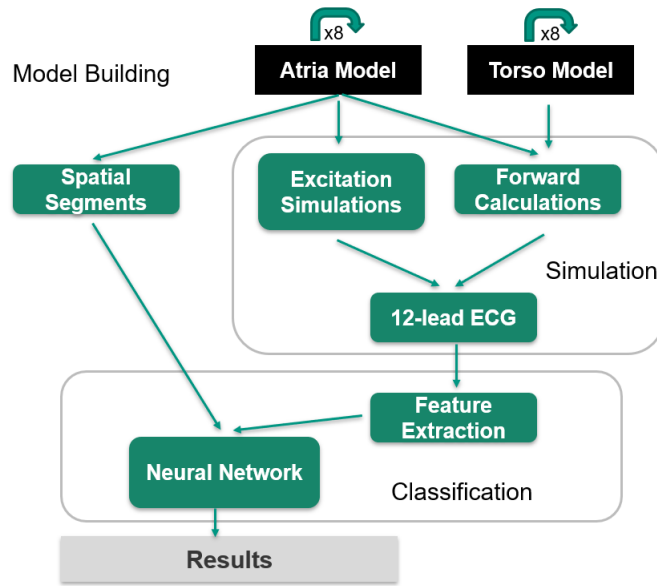


Figure 1.1: Diagram which represents the workflow followed in this thesis.

1.2 Goal of this Research

The aim of this thesis is to study, whether the standard 12-lead ECG can be used to localize the origin of atrial ectopic beats, in spite of recent studies declaring that the standard 12-lead ECG might not provide sufficient information to localize foci. [1] We use an electrophysiological atria-torso model together with a NN to develop a pipeline to classify 12-lead ECG signals into segments associated with ectopic atrial sites.

First of all, the main task to resolve our problem is to split the atria into spatial segments. Recent studies have focused on the segment creation using clustering and statistical procedures. In this thesis, we develop a new automatic method to create segments that is only based on geometrical landmarks and the geometry itself. Excitation simulations and forward calculations are then performed to yield ECG signals. Finally, a NN is developed, able to classify ECG signals into the predefined spatial segments of the atria. This workflow is represented in Figure 1.1

1.3 Outline

This thesis is structured as follows.

- The physiological fundamentals of the heart needed to understand this work are explained in chapter 2.
- The mathematical fundamentals of atria modeling, principal component analysis (PCA), FastICA and NNs are given in chapter 3.
- Chapter 4 describes the different atria-torso models used in this thesis.

-
- Chapter 5 presents the methods to segment the atria, extract the ECG features and build the NNs.
 - The results of the segmentation are presented and analyzed in chapter 6.
 - The results of the classification with the NNs are presented and analyzed in chapter 7.
 - A conclusion is drawn in chapter 8.
 - Finally, a discussion of the results and an outlook on possibilities for future work is given in chapter 9.

PART I

FUNDAMENTALS

Medical Fundamentals

The heart is a muscular organ that contracts and relaxes rhythmically and hence drives the circulation of blood throughout the body. In every heartbeat, an electrical current advances through the heart, which triggers myocardial contraction. The result is a coordinated pattern which leads to coordinated systole. The resulting change in potential difference on the body surface is known as ECG.

Understanding the basis of a normal ECG requires recognition of three phenomena: the electrophysiology of cells, the propagation of electrical excitation through the heart, and how that leads to potentials on the body surface.

2.1 Cardiac Anatomy

The heart distributes oxygen and other nutrients provided within the blood to all organs and muscles. In humans, the heart is split into four chambers (see Figure 2.1). [7]

The heart drives two serially connected circulations, the pulmonary and the systemic circulation. Four valves block the blood from running into the wrong direction. The RA receives deoxygenated blood through the superior and inferior caval veins. The LA receives oxygenated blood through four pulmonary veins. When the ventricles contract (systole) the blood inside the right ventricle (RV) is ejected through the pulmonary arteries to the lungs, while the blood inside the left ventricle (LV) is ejected through the aorta to the rest of the body. When the ventricles relax (diastole) blood received from the veins flows through the atria into the ventricles. When the atria contract, further blood is pushed into the ventricles (active filling).

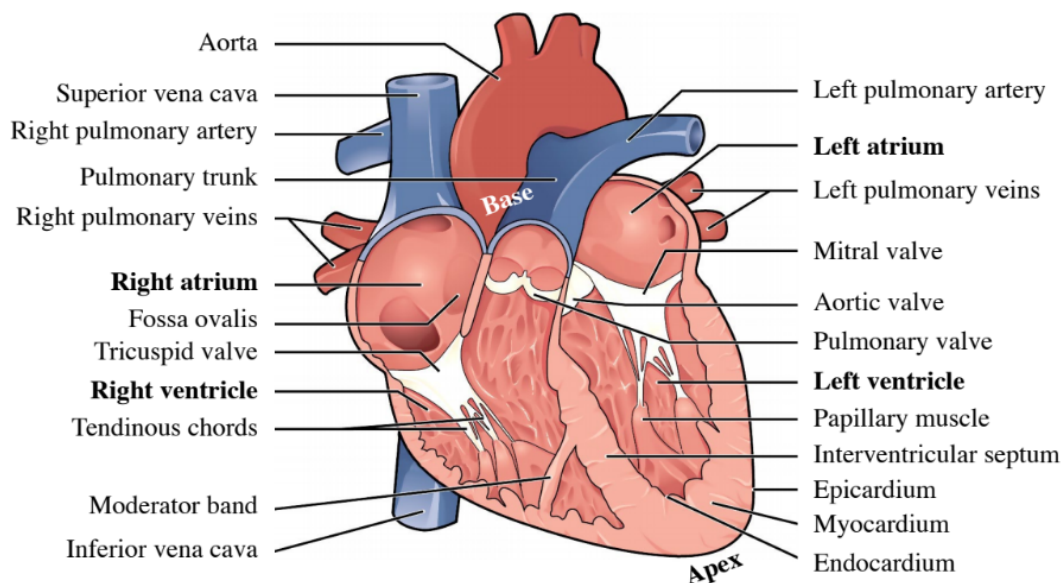


Figure 2.1: Illustration of the human heart. Figure inspired by [7].

2.2 Cardiac Physiology

Each mechanical heartbeat is triggered by an action potential that is conducted rapidly throughout the organ to produce a coordinated contraction. The cell membrane controls permeability to a number of ions, which pass across the membrane through specific ion channels that can open and close. These channels are gated channels and their opening and closing occurs in response to changes in the transmembrane voltage. [8]

Before the action potential is propagated, it must be initiated by pacemakers, cardiac cells that possess the property of automaticity. Such cells are found in the sino-atrial node (SA). Under normal operating conditions, the SA node determines heart rate. However, in some pathologic circumstances, the rate of lower pacemakers can exceed that of the SA node, and then e.g. the AV node as secondary pacemaker determines the overall heart rate.

An action potential propagates along the cell membrane until the entire cell is depolarized. Myocardial cells have the unique property of transmitting action potentials from one cell to adjacent cells by means of direct current spread. Thus, an impulse originating anywhere in the myocardium will propagate throughout the heart, resulting in a coordinated mechanical contraction.

2.3 The Physical Basis of Electrocardiography

The electrical activity of the cells and current flows within the body lead to potential differences on the torso surface, resulting in the ECG. The simplest mathematical model for the ECG is the single dipole model, which has two components, a representation of the

electrical activity of the heart, and the geometry and electrical properties of the body. In the heart, there is an associated intracellular current generated in the direction of propagation (current dipole). There is also an equal extracellular current flowing against the direction of propagation, and so charge is conserved. [8]

Current dipoles are distributed in space, but the total electrical activity of the heart may be represented as a single equivalent dipole, $M(t)$, whose magnitude and direction is the vector summation of all the dipoles. The heart vector changes in magnitude and direction as a function of time.

The resulting surface distribution of currents and potentials depends on the electrical properties of the torso. As an approximation, the model ignores anisotropy and inhomogeneity of the torso. Laplace's equation gives the potential distribution on the torso. More generally, the potential difference between the two points on the surface of the torso is

$$V_{AB}(t) = M(t) \cdot L_{AB}(t) \quad (2.1)$$

where L_{AB} is known as the lead vector connecting points A and B on the torso. Potentials, Θ , are usually referenced to a reference electrode at the lower right part of the torso or to the average of potentials at both arms and the left leg (Wilson central terminal).

$$\Theta_{CT}(t) = (\Theta_{RA}(t) + \Theta_{LA}(t) + \Theta_{LL}(t))/3 \quad (2.2)$$

where RA indicates right arm, LA indicates left arm, and LL indicates left leg.

2.3.1 The Normal ECG

The performance of the heart as a pump is dependent primarily of the myocardium. Other factors include: the geometric organization of the myocardial cells, the properties of the cardiac tissue and the heart's electrical rhythm. The LA and left ventricle form the left heart. As noted earlier, under normal conditions the atria finish contracting before the ventricles begin contracting. [8]

The six precordial leads require that six electrodes are placed around the torso (Figure 2.2), and the ECG represents the difference between each of these electrodes (V1–6) and the reference potential. Additional electrodes, the limb leads, are placed on each of the subject's four extremities. The three classical limb leads are defined as follows:

1. Lead I, the difference between left arm and right arm.
2. Lead II, the difference between the left leg and the right arm.
3. Lead III, the difference between the left leg and the left arm.

The augmented limb leads represent the potential at a given limb with respect to the average of the potentials of the other two limbs. aVF is the difference between the left leg and average of the arm leads; aVR is the difference between the right arm and the average of left leg and

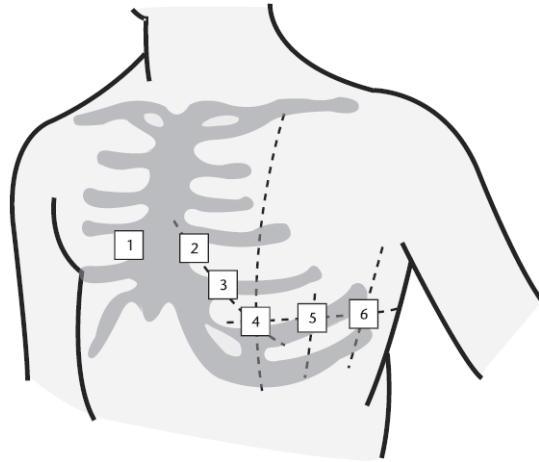


Figure 2.2: The six standard chest leads. Figure inspired by [8].

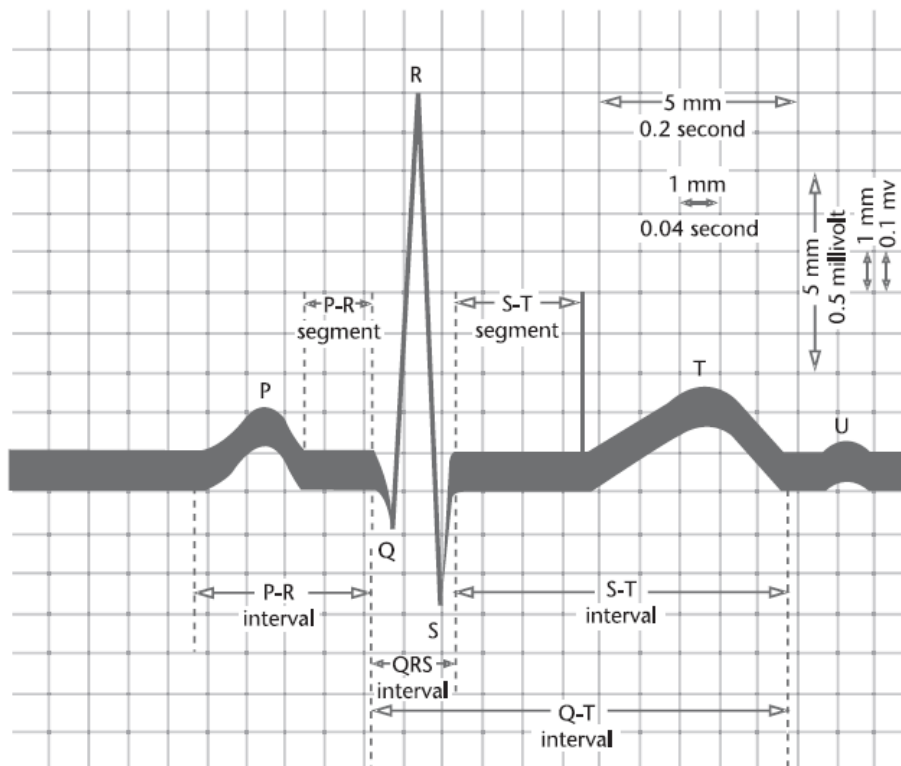


Figure 2.3: Normal features of the ECG. Figure inspired by [8].

left arm, and aVL is the difference between the left arm and the average of the right arm and left leg.

Figure 2.3 illustrates the normal clinical features of the ECG, which include wave amplitudes and interwave timings. The locations of different waves on the ECG are arbitrarily marked by the letters P, Q, R, S, and T (and sometimes U, although this wave is often hard to identify,

as it may be absent, have a low amplitude, or be masked by a subsequent beat). The values for the clinical features indicated on the graph in Figure 2.3 are typical, although they can vary based upon gender, age, activity, and health.

Mathematical Fundamentals

In the following sections, different algorithms and methods are introduced. They comprise techniques for calculating shortest paths on curved geometries as well as methods needed for feature extraction and classification with NNs.

3.1 The Fast Marching Method

Fast Marching Methods [9] are numerical algorithms for solving the nonlinear Eikonal equation

$$\|\nabla u(x)\| = F(x) \text{ in } \Omega, F(x) > 0 \quad (3.1)$$

Here, Ω is a domain in R^n , and the right-hand side $F(x) > 0$ is typically supplied as a known input to the equation, as is the boundary condition that u equals predefined values in a specific region Γ on the surface of Ω . If $F(x)$ equals one and u is zero on the boundary Γ , u represents the shortest distance to the boundary. If $F(x)$ is the reciprocal of a velocity, u represents the time of arrival.

The Fast Marching Method is connected to Huyghen's principle, which is a construction involving expanding wavefronts, and Dijkstra's method, which is an algorithm for computing smallest cost paths on a network. Dijkstra's method keeps track of the current smallest cost for reaching a grid point and fans out along the network links to touch the adjacent grid points. The Fast Marching Method exploits the same idea in the context of an approximation to the underlying partial differential equation, rather than the discrete network links.

To solve the equation, suppose the solution is known at a set of points. For every not-yet-accepted point we compute a trial solution by using the given values for u at known points and values of $F(x)$ at all other points. We now observe that the smallest of these trial solutions must be correct, because it depends only on accepted values that are themselves smaller. The complete procedure is given in Algorithm 3.1.

Algorithm 3.1 The fast marching method. $\mathcal{F}(X)$ denotes the neighborhood of X . [10]

```

while  $TRIAL \neq \emptyset$  do
   $X \leftarrow \operatorname{argmin}_{X \in TRIAL} \{t_a(X)\}$ 
   $TRIAL \leftarrow TRIAL \setminus \{X\}$ 
   $KNOWN \leftarrow KNOWN \cup \{X\}$ 
  for all  $(X_i \in \mathcal{F}(X)) \wedge (X_i \notin KNOWN)$  do
     $t_a(X_i) \leftarrow \operatorname{update}(X_i, X)$ 
    if  $X_i \notin TRIAL$  then
       $TRIAL \leftarrow TRIAL \cup \{X_i\}$ 
    end if
  end for
end while

```

3.2 Geodesic

A geodesic is the generalization of a straight line to curved surfaces. It is the curve on a surface in three-dimensional space, for which the normal of the curve equals the normal of the surface [11]. On triangle meshes, an approximate geodesic from a point A to a point B can be obtained by using the fast marching method to calculate a distance map originating from A and then performing gradient descent starting from B [12].

3.3 Principal Component Analysis

The central idea of PCA [13] is to reduce the dimensionality of a data set consisting of a large number of interrelated variables, while retaining as much as possible of the variation present in the data set. This is achieved by transforming to a new set of variables, the principal components, which are uncorrelated, and which are ordered so that the first few retain most of the variation present in all of the original variables.

The following description is taken from [14]. A data matrix, \mathbf{X} , with column-wise zero empirical mean, where each of the n rows represents a different repetition of the experiment, and each of the p columns gives a particular kind of feature. The transformation is defined by a set of p -dimensional vectors of weights $\mathbf{w}_{(k)} = (w_1, \dots, w_p)_{(k)}$ that map each row vector $\mathbf{x}_{(i)}$ of \mathbf{X} into a new vector of principal component scores $\mathbf{t}_{(i)} = (t_1, \dots, t_l)_{(i)}$, given by

$$t_{k(i)} = \mathbf{x}_{(i)} \cdot \mathbf{w}_{(k)} \quad \text{for} \quad i = 1, \dots, n \quad k = 1, \dots, l \quad (3.2)$$

in such a way that the individual variables t_1, \dots, t_l of \mathbf{t} considered over the data set successively inherit the maximum possible variance from \mathbf{x} , with each loading vector \mathbf{w} constrained to be a unit vector.

3.3.1 Dimensionality reduction

The transformation $\mathbf{T} = \mathbf{X}\mathbf{W}$ maps a data vector $x_{(i)}$ from an original space of p variables to a new space of p variables which are uncorrelated over the dataset. Keeping only the first L principal components yields:

$$\mathbf{T}_L = \mathbf{X}\mathbf{W}_L \quad (3.3)$$

where the matrix \mathbf{T}_L now has n rows but only L columns. In other words, PCA learns a linear transformation $t = \mathbf{W}^T x, x \in \mathbb{R}^p, t \in \mathbb{R}^L$, where the columns of the $p \times L$ matrix \mathbf{W}_L form an orthogonal basis for the L features that are decorrelated.

Such dimensionality reduction can be a very useful step for visualizing and processing high-dimensional datasets, while still retaining as much of the variance in the dataset as possible.

3.4 FastICA

FastICA is an algorithm for independent component analysis [15]. It seeks an orthogonal rotation of prewhitened data, through a fixed-point iteration scheme, that maximizes a measure of non-Gaussianity, which serves as a proxy for statistical independence, of the rotated components.

The following description is taken from [16]. Let the $\mathbf{X} := (x_{ij}) \in \mathbb{R}^{N \times M}$ denote the input data matrix, M the number of columns corresponding with the number of samples of mixed signals and N the number of rows corresponding with the number of independent source signals. The input data matrix \mathbf{X} must be prewhitened, or centered and whitened, before applying the FastICA algorithm to it.

The iterative algorithm finds the direction for the weight vector $\mathbf{w} \in \mathbb{R}^N$ that maximizes a measure of non-Gaussianity of the projection $\mathbf{w}^T \mathbf{X}$ with $\mathbf{X} \in \mathbb{R}^{N \times M}$ denoting a prewhitened data matrix as described above. The steps for extracting the weight vector \mathbf{w} for single component in FastICA are the following:

1. Randomize the initial weight vector \mathbf{w}
2. Let $\mathbf{w}^+ \leftarrow E \{ \mathbf{X}g(\mathbf{w}^T \mathbf{X})^T \} - E \{ g'(\mathbf{w}^T \mathbf{X}) \} \mathbf{w}$
3. Let $w \leftarrow \mathbf{w}^+ / \|\mathbf{w}^+\|$
4. If not converged, go back to 2

3.5 Supervised Learning Methods for Classification / Neural Networks

The application of NN methods has become an important trend [8]. A NN model can be used to build different models, using different classifier networks or different preprocessing

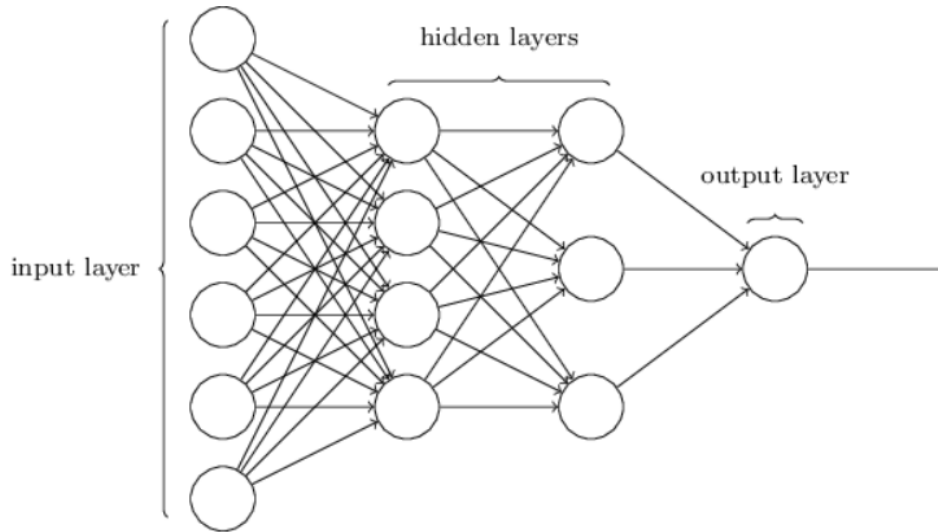


Figure 3.1: Example architecture of a MLP. Figure inspired by [8].

methods of the data. In practice, often multiple realizations are implemented and tested and the best one is chosen.

The components of the input vector x , contains the features representing the input applied to the classifiers. The learning process is based on a set of learning pairs (x_i, d_i) , where x_i represents the vector of features and d_i is the vector of class codes.

The multilayer perceptron (MLP) (detailed in Figure 3.1) consists of many simple neuron-like processing units of sigmoidal activation functions grouped together in layers. A typical network contains one hidden layer followed by the output layer of neurons. Before training, the weights are initialized randomly. The network is then trained to produce a desired output vector d_i when presented with an input vector x_i . This procedure changes the weights of all neurons until the network produces the desired output within a given tolerance.

The most effective learning methods rely on gradient methods. Gradient vectors in a multilayer network are computed using the backpropagation algorithm. In the gradient method of learning, the weight vectors w are adapted from cycle to cycle according to the information of gradient of the error function.

$$w(k+1) = w(k) + \eta p(k) \quad (3.4)$$

where η is the learning constant calculated at each cycle and $p(k)$ is the direction vector of minimization in the k th cycle.

After finishing the training phase, the obtained weights are fixed and ready for use in the test, in which an input vector, x , is processed by the network to generate the output neuron signals responsible for class recognition. It should be observed that the gradient approach to learning leads to the local minimum of the objective function. If this value is not acceptable, the learning process may be repeated starting from different initialization of weights.

Generalization is a fundamental property that should be sought in practical applications of neural classifiers. It measures the ability of a network to recognize patterns outside the

training set. If the number of weights of the network is too large and/or the number of training examples is too small, then there will be a vast number of networks which are consistent with a training data, but only a small set which accurately fits the true solution space. Hence, poor generalization is likely. A common sense rule is the cross-validation technique, where the data are divided into training, validation, and testing sets. The validation set is used to check the generalization ability of the network learned on the training data. The test set error is not used during training, but it is used to compare different models. The size of the network corresponding to the minimum validation error is accepted as the optimal one.

PART II

METHODS

Materials

Computational models of the heart [17] [18] have evolved to become an important tool for understanding several types of cardiac disorders like AFib, atrial flutter or ventricular arrhythmias. A comprehension of AFib can be supported by tuning electrophysiological parameters like conduction velocity (CV) and by triggering extrasystoles from various regions in a macroscopic model of the human heart.

The activation pattern of the atria is strongly dependent on their anatomical properties [10]. Moreover, mechanisms of arrhythmia initiation and perpetuation interfere with the atrial shape. Therefore, a realistic model of human atrial anatomy is required to study such phenomena. If the BSPM or ECG is of interest, also a torso model is required.

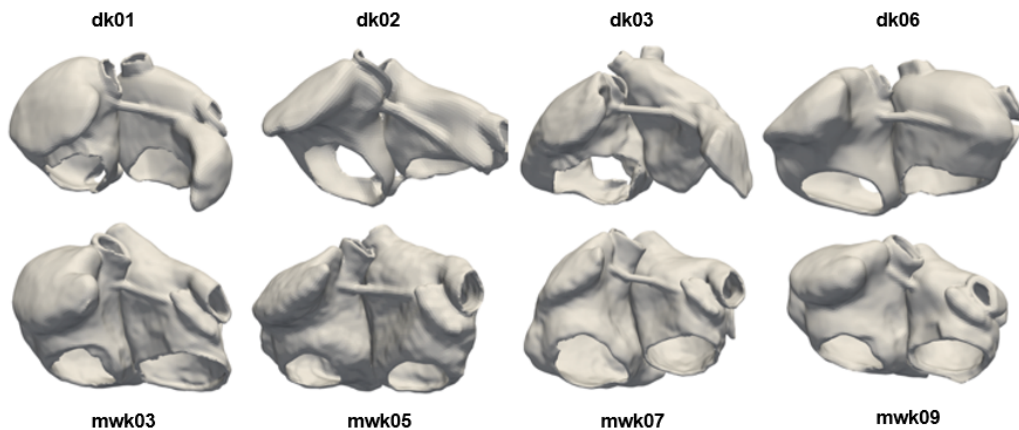


Figure 4.1: Models of the eight individual atria used in this thesis.

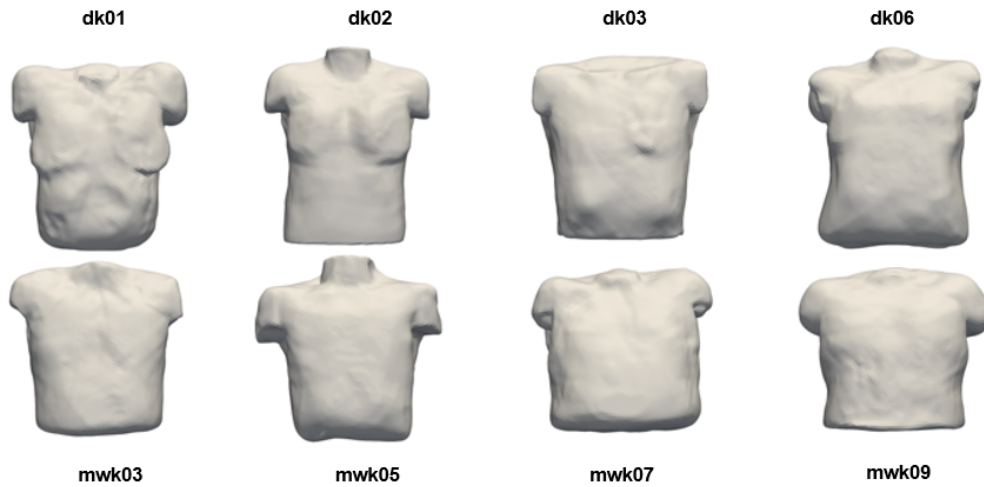


Figure 4.2: Models of the eight individual homogeneous torsos used in this thesis.

4.1 Atria models

A geometrical model of the atria is a 3D object that includes the thickness of the atrial wall. Also, adequate meshes with smooth surfaces at the boundaries between different tissue classes, are needed for numerical simulations.

While very detailed microstructure-based models of single regions of the atria exits, they represent only their shape normally. 3D models of the atria can be divided into volumetric models comprising an atrial wall with a finite thickness and surface models. Another important feature is the conductive properties of the septum. [10]

Within the scope of this thesis, a virtual population of eight atria models (see Figure 4.2) presented by Krueger et al. was used [19]. In this thesis, triangle meshes were derived from original voxel segmentations and tetrahedralized for excitation simulations.

4.2 Torso models

The methods for resolving the potentials on the thorax require an accurate description of the involved volume conductor effects. These entail the position and orientation of the heart, the geometry of the thorax, the location of the electrodes on the thorax, and the parts of the thorax where the electrical conductivity differs substantially from that of the surrounding tissue.

Volume conductor effects govern the propagation of the electric currents throughout the thorax that generate the electric potential differences. One of the most important questions

Table 4.1: Influence of the conductivity values in different model compartments, documented by the resulting relative difference (64 leads) between the simulated signals and the reference (fully inhomogeneous model). Table inspired by [20]

Conductivity values (S/m)			
Lungs	Thorax	Cavities	Relative difference
0.04	0.2	0.6	0
0.2	0.2	0.6	0.39
0.04	0.2	0.2	2.22
0.2	0.2	0.2	1.89

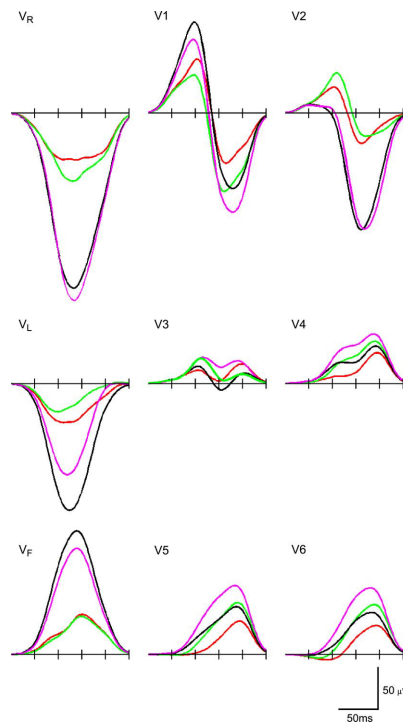


Figure 4.3: The influence of discarding different inhomogeneities on some of the lead potentials. Red: results based on the fully inhomogeneous (reference) model. Green: discarding lungs, Black: discarding cavities, Magenta: discarding lungs and cavities (homogeneous thorax). Figure inspired by [20].

regarding the volume conductor it is how the major inhomogeneities in the body affect the P wave morphology and amplitude.

The torso models conductivity values were based on the study of Peter van Dam et al. [20]. This study which tested the torso inhomogeneities, shows that the blood cavities play a major role in the determination of P wave morphology and amplitude. Although [20] shows that it is important to especially include blood volumes, for simplicity we decided to use a homogeneous torso model with a conductivity of 0.2 S/m, shown in (Table 4.1 and Figure 4.3). If the results of this thesis are successful, a new heterogeneous torso model could be used as a future improvement of the classification in real data.

In this thesis we used the homogeneous thorax data for subject 1–8 which were manually segmented using deformable surface meshes by Krueger et al. [19].

Methods

This chapter introduces the methods used to resolve the classification of atrial ectopic beats into spatial segments in a chronological order. The first section is based on the definition of atrial segments, together with the torso combination to create simulated 12-lead ECG signals to be classified. The next section, torso forward calculations, introduce how the electrical signals are propagated through the human torso. Finally, a signal feature extraction is performed to extract the inputs needed for the NN classifier.

5.1 Left and Right atrium separation

Before the creation of atrial segments, it is essential to separate between LA and RA. One of the biggest problems of this separation is the wall between LA and RA, known as the primary septum, and the bridges connecting both atria.

To solve this problem, this thesis presents two different approaches, both based on an initial division of epicardium and endocardium surfaces. Note that from this point on, all segments created in this thesis are created on the epicardium. Because of this reason, it is important to divide the 3D atria model into both layers.

The first step to solve the LA and RA separation is extracting the endocardium layer. To achieve this task we follow the methodology shown in Figure 5.1. First of all, the location of the atria veins is needed in the separation algorithm, because they join endocardial and epicardial layers. Selecting and cutting the rings around the veins in both atria helps us to divide the 3D atria model. This is done manually in all models using Blender.

Once we have the separation between both layers, the endocardium is used to separate between LA and RA. The important property of the endocardial layer is that it is already divided between LA and RA endocardium. In the next subsections, both approaches to LA and RA separation are described.

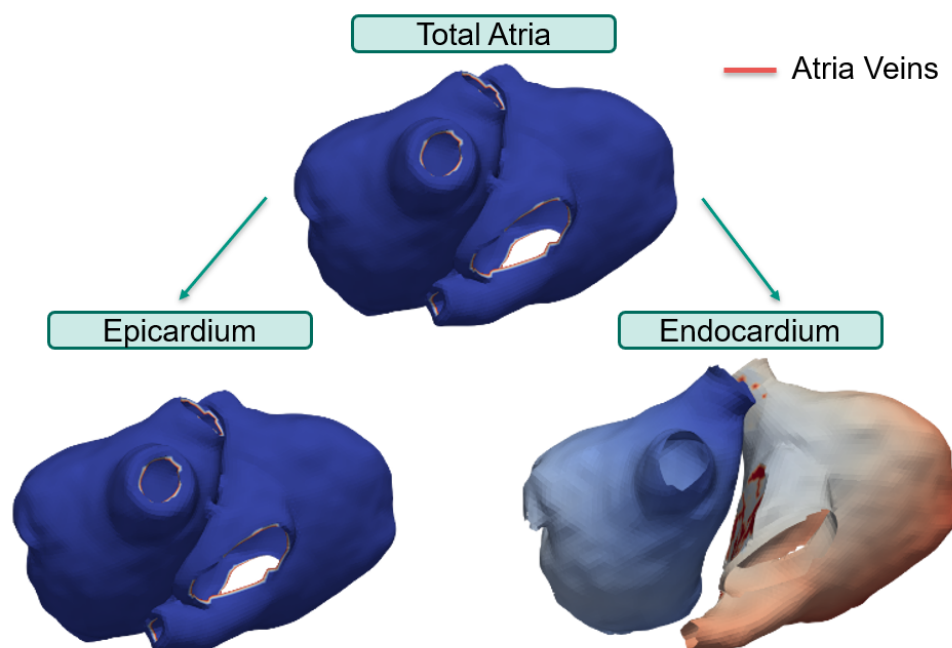


Figure 5.1: Epicardium and endocardium separation using the atria model. The red color line represents the vein indexes.

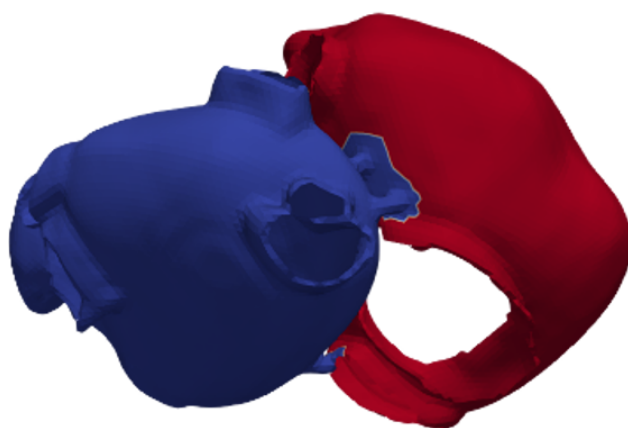


Figure 5.2: Nearest neighbor LA and RA separation approach. LA is marked in blue color and RA is marked in red.

5.1.1 Nearest neighbor approach

The first approach is based on the nearest neighbor algorithm. For every epicardial point, it is checked, whether the euclidean distance to one of the LA or any of the RA endocardial points is smaller than the rest.

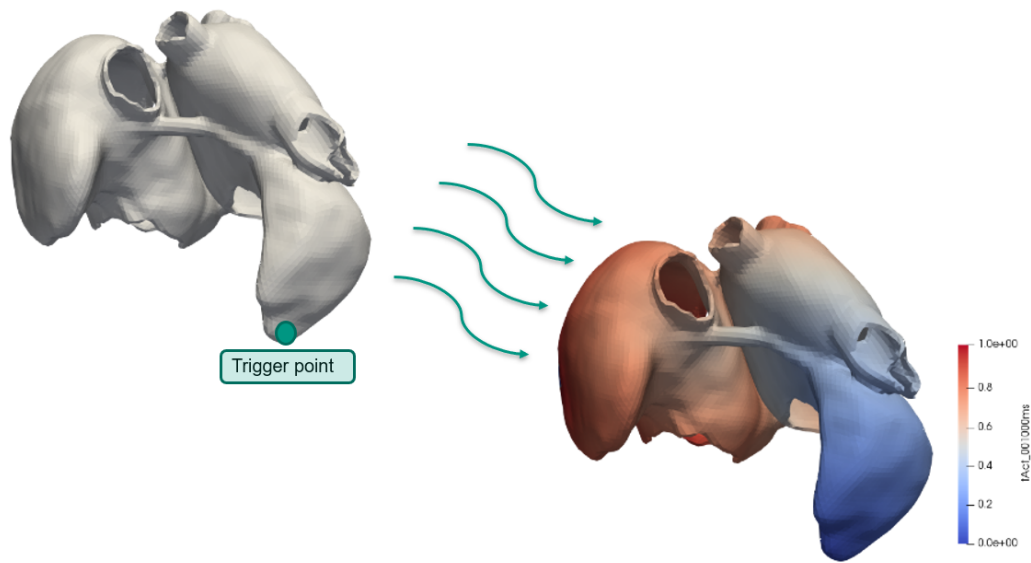


Figure 5.3: Fast marching trigger point simulation through the atria model. Blue color represents small activation time. On the other hand, the red color represents large activation time.

The result of this approach is shown in Figure 5.2. The LA is marked in blue color and the RA is marked in red color. Misclassification between LA and RA can be seen in the connecting bridges of the septum. This misclassification is relevant for the creation of segments because a segment can not belong to both atria. In order to evade this problem, a new approach is discussed in the next section.

5.1.2 Fast-marching-based approach

The error in the division between both atria needs to be avoided. Therefore, a new approach based on running the fast marching algorithm (see section 3.1) on tetrahedral meshes is presented.

Before the explanation of the solution, it is important to give an overview of how the fast marching simulations look like. In the left part of Figure 5.3, a trigger point on the LA appendage is selected as the initial input of the algorithm. After that, the simulation runs with CV as parameter. The value of the neighbor nodes is calculated and the algorithm propagates the simulation through all the nodes on the atria. In the right part of Figure 5.3 we are able to see the result of the simulation. Blue colors represent the nodes with the lowest activation time. On the other hand, red colors represent the ones with highest activation time. Different trigger points generate different results.

Now the new approach to divide LA and RA shall be presented. The following steps are needed to solve the problem:

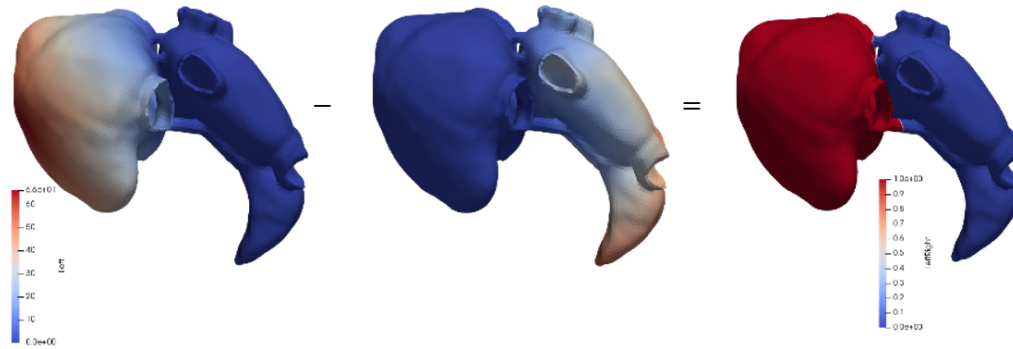


Figure 5.4: Tetrahedral mesh LA and RA separation approach. Firstly, the fast marching is running with LA endocardium points as trigger points. Secondly, this time subtract the simulation with RA endocardium points as trigger points. Finally, the application of a zero threshold is able to divide LA (blue) and RA (red)

- Use of the volumetric 3D atria model in this approach. Simulations start from endocardium points, propagating them through tetrahedral meshes until the epicardium is reached.
- Fast marching simulation using the LA endocardium points as trigger points. Keep the resulting activation times of every atria node as T_{left} .
- Fast marching simulation using the RA endocardium points as trigger points. Keep the resulting activation times of every atria node as T_{right} .
- Create a new time vector: $T_{left/right} = T_{left} - T_{right}$.
- Apply a zero threshold, $thr = 0$, to divide left and right parts. LA epicardium points are the epicardium points below the threshold. RA epicardium points are the ones up to the threshold. The summary of this approach is shown in Figure 5.4.

Finally, an accurate separation between LA and RA is achieved. Figure 5.5 shows the separation. If we take a look at the septum and the connecting bridges, we can see the precision differentiating LA and RA in the bridges. With this approach, we are able to create segments that do not belong to both atria. In conclusion, the fast marching separation performs better than the nearest neighbor. This is the reason why we used fast marching mesh separation.

5.2 Atria segmentation

The high anatomical variability of the atria makes its segmentation a particularly difficult problem. Specifically, the asymmetrical parts of the RA. Due to the fact that the RA and especially the right atrial appendage are located near the body surface, any change in their

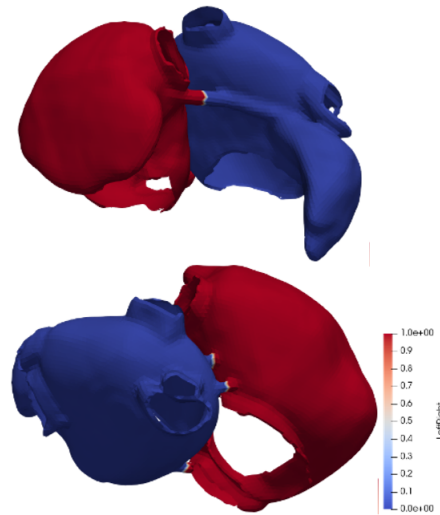


Figure 5.5: Tetrahedral mesh LA and RA separation approach. LA is marked in blue color and RA is marked in red.

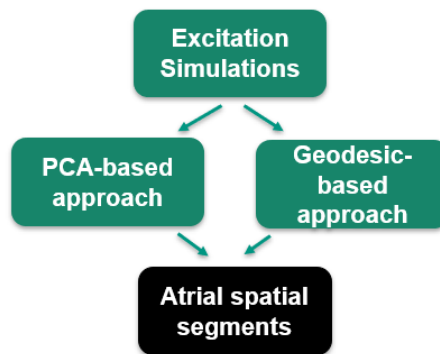


Figure 5.6: Approaches to automatically create atrial spatial segments.

shape may affect the potentials on the body surface. The effect of this displacement on 12-lead ECG is a topic of our current research. Also, the shape of the LA, as well as the number and locations of the pulmonary veins connecting to it, vary substantially across subjects. Figure 5.7 shows the challenge of segment creation. This challenge could be solved in multiple ways. Most existing approaches are based on clustering. However, it is not easy to transfer clustering results to another geometry. Therefore, we decided to use a purely geometric approach to define segments. We based our segment-division on robust landmarks that exist in every atrial geometry: the orifices of pulmonary veins and caval veins.

In this section we discuss two different approaches, shown in Figure 5.6, to develop an individual-independent segments creation, the first one uses PCA and the second one is directly based on the geometrical aspects of the model, and it will be called "geodesic-approach" in the following section.

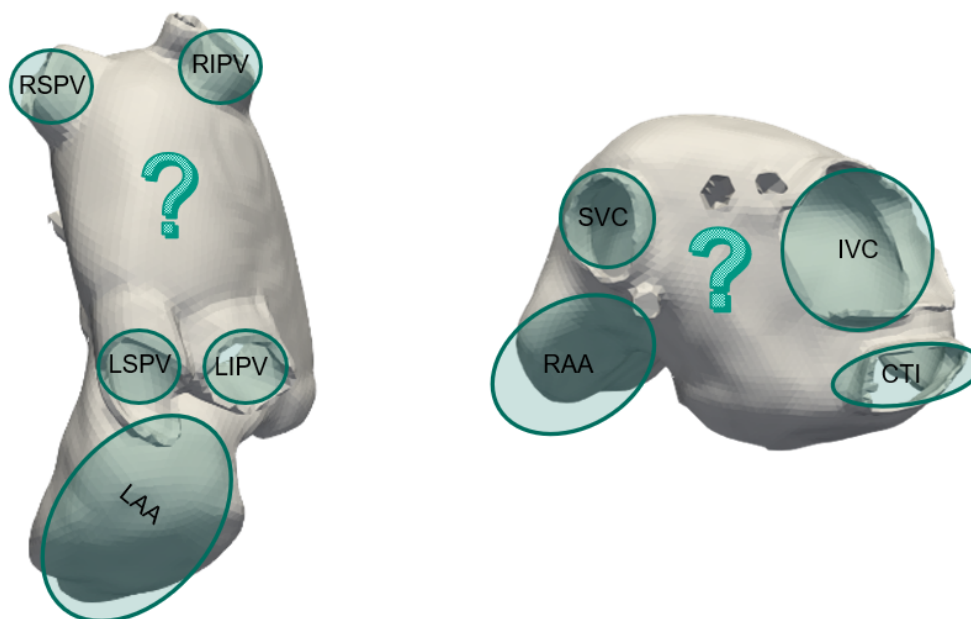


Figure 5.7: Representation of the segments creation challenge. The figure marks the most important veins and locations of the atria.

5.2.1 PCA-based approach

One of the possible approaches to define segments on the atria could be the incorporation of linear independent components. Basically, the main approach to reach this purpose is the application of PCA to the local activation times resulting from different stimulation locations. The basics of the PCA algorithm are explained in chapter 3. This linear transformation reduces the dimension of the data, while still retaining as much of the variance in the dataset as possible. Applied to the segmentation, PCA could be useful to see similar patterns between different atria models. If the principal components have the same pattern between different models, they can easily be used for defining segments.

The algorithm is implemented in the following way:

- Calculation of activation times in the atria for around 300 stimulation triggers equally distributed on the atria using fast marching.
- Application of the PCA to the activation times.
- Selection of the principal components that represent the original data with 95% of variance. Selecting the first 4 principal components, 95% of variance is included in all the different geometries.

Applying the PCA to equally distributed triggers around the atria in different 3D models results in:

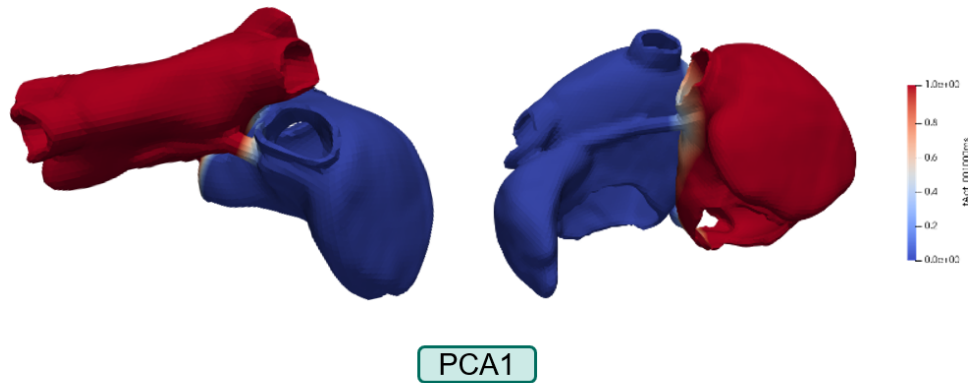


Figure 5.8: PCA first component in two different atria models after running several ectopic triggers in the atria. A gradient between LA and RA can be seen.

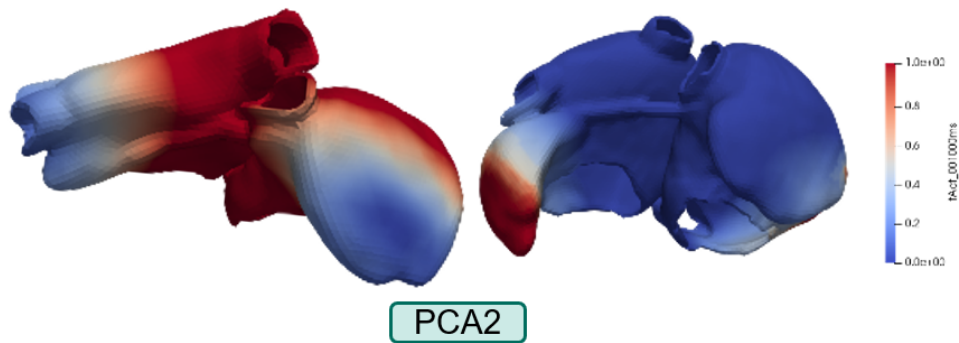


Figure 5.9: PCA second component in two different atria models after running several ectopic triggers in the atria. No clear gradient direction can be seen.

- The first principal component represents the highest variance, meaning that it is the single component which represents the data the best. Figure 5.8 shows the geometrical representation of the first principal component. There are two different geometries represented in this picture. Both of them separate in a useful way LA and RA. We could use also this approach to separate both atria, but, the bridge connection is not well differentiated (the same error could be appreciated with the nearest neighbor approach Figure 5.2).
- The pattern of the second principal component is not clear to interpret in Figure 5.9. In the atria model of the left, it divides the inner part of the atria (septum and his nearest segments) from the outer part of the atria (appendages). On the other hand, in the model on the right, it divides LA appendage (LAA) from the rest of the atria. In conclusion, the second principal component has not a similar pattern between different geometries.

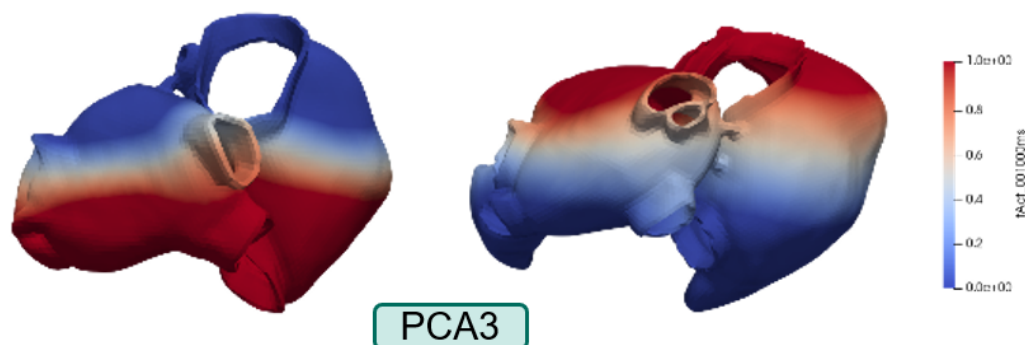


Figure 5.10: PCA third component in two different atria models after running several ectopic triggers in the atria. An anterior-posterior gradient can be seen.

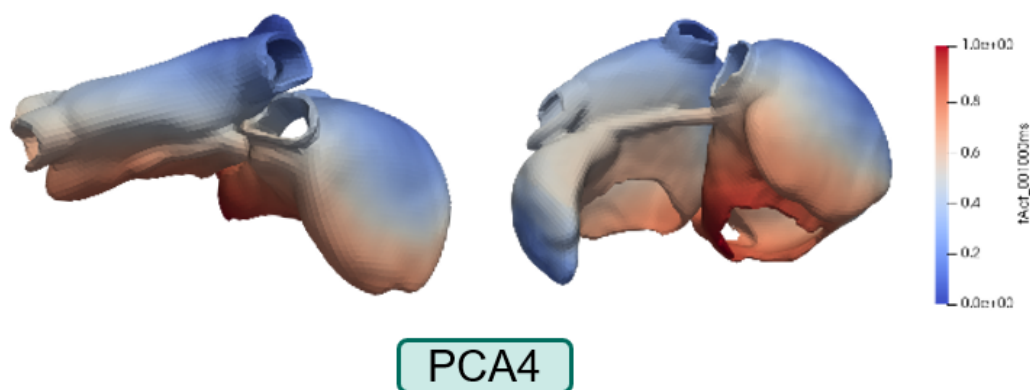


Figure 5.11: PCA four component in two different atria models after running several ectopic triggers in the atria. An inferior-superior gradient can be seen.

- Figure 5.10 shows the third principal component applied to two different geometries. Although a clear gradient between anterior and inferior sides can be seen, the accuracy is poor and it is not a reliable method to apply between different geometries.
- Finally, the fourth principal component is represented in Figure 5.11. Although an inferior-superior gradient shown for the two geometries, this one is the principal component with the highest irregular pattern between geometries. Here it is really difficult to identify a similar pattern between both geometries. We discard automatically the use of the fourth principal component.

Despite the fact that the application of PCA to find similar patterns cannot be used for segment creation, it is very useful to know how these patterns look like to create the segments and proceed with the next approach.

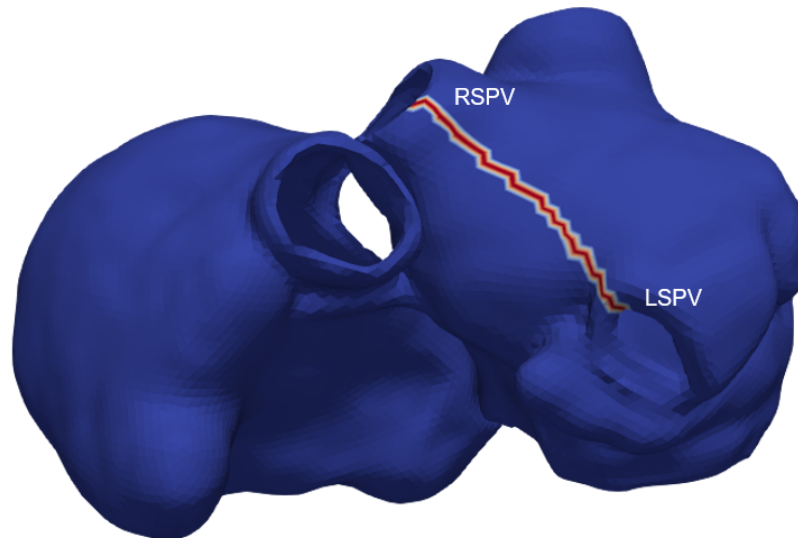


Figure 5.12: Representation of a geodesic path in the atria. This figure shows the geodesic path between the RSPV and the LSPV marked in red color.

5.2.2 Geodesic-based approach

As we have discussed in the last section, the PCA approach is not satisfactory for segment creation. In place of PCA, we decided to apply a procedure based on the atria geometry itself. The algorithm to create these segments is automatically developed in MATLAB. It is useful because it can easily be applied to new future 3D geometries. The input variables are: atria 3D geometry and node indexes defining each of the 6 veins and 2 atrio-ventricular orifice rings. With only this information, it is possible to automatically segment new atrial geometries and build a more robust database to improve our classification.

In the next subsections, we discuss the segment creation on the LA and RA. We decided to start with LA because it is more important clinically, foci occur more frequently around the pulmonary veins than in other parts. Later on, we discuss the segmentation of RA, which is more asymmetrical than the LA, and there are fewer studies about the segmentation.

5.2.2.1 LA segments

Clinically, LA segmentation is a highly relevant problem. The high anatomical variability of the LA shape and the pulmonary veins presents significant difficulties for cardiac ablation. In this thesis, we demonstrate fully-automatic non-parametric geodesic-based definition of segments of both the atrial body and pulmonary veins connected to it on a set of 8 atria models. Our method captures all of the pulmonary veins as well as the atrium appendages in all the models.

Experimental results illustrate the capacity of our method to handle high anatomical variability, yielding accurate segmentation and detecting all pulmonary veins in all subjects, as

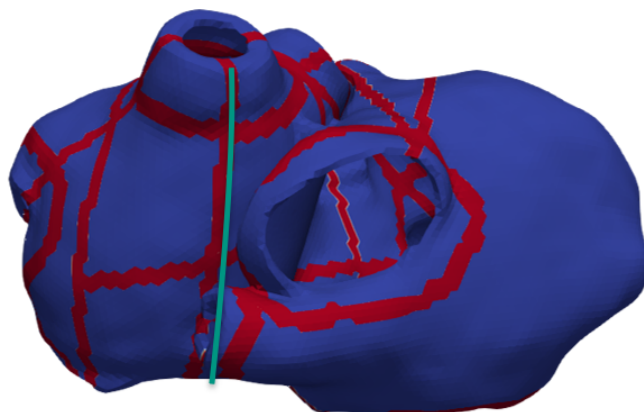


Figure 5.13: Segment boundaries following the geodesic path approach in the LA. The boundary marked in green color has been created using a geodesic path between LSPV and one fixed point in the MV.

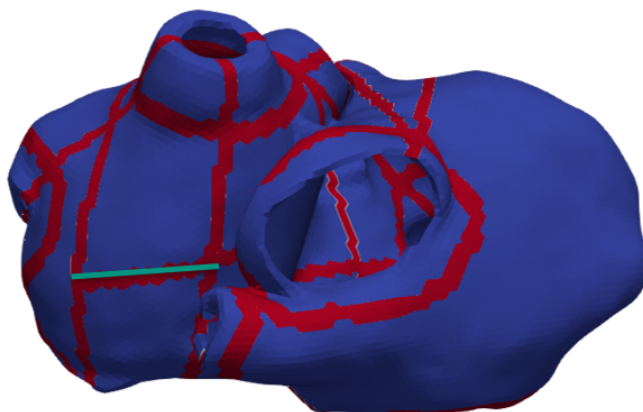


Figure 5.14: Segment boundaries following the artificial geodesic path approach in the LA. The boundary marked in green color has been created using a geodesic path between two original geodesic paths (one path from the mid-point of the pulmonary veins to the MV and the other starting from the RIPV to the MV).

well as left atrial appendage (LAA) and right atrial appendage (RAA). In addition automatic segmentation might help in planning of cardiac ablation, and can also assist in the evaluation of the procedure outcome.

The segmentation of the LA has a high level of freedom, but with a few limitations:

- Important clinical veins and locations of the atria need to be segmented in different segments. In this case: pulmonary veins and appendages.
- One segment cannot belong to LA and RA at the same time.
- Boundaries between segments need to be clearly differentiated.

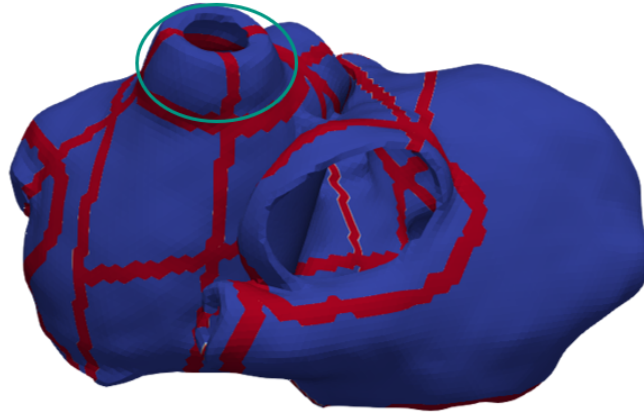


Figure 5.15: Segment boundaries following the time activation threshold approach in the LA. The boundary marked in green color has been created using a time activation threshold depending on the mid-point between pulmonary veins. This threshold is always fixed to give consistency between geometries.

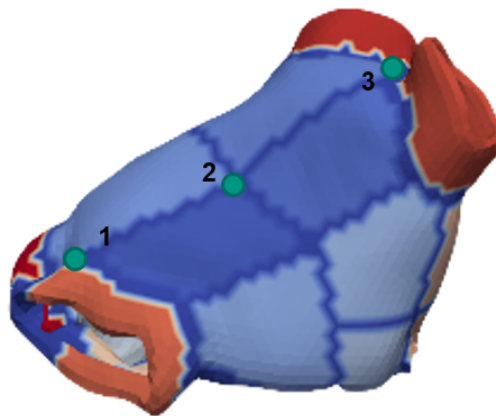


Figure 5.16: Pulmonary veins segment boundaries following the time activation threshold approach in LA. To configure the threshold it is necessary to establish some points which work as triggers. The point number 1 is used to limit the segment boundary between LIPV and RIPV. The point number 3 is used to limit the segment boundary between LSPV and RSPV. Finally, the point number 2 is used also in both configurations to avoid the penetration of the boundaries in the posterior wall between inferior pulmonary veins and superior.

- Segmentation needs to be consistent between different atria geometries.

Keeping in mind all of these limitations, we proceed with the LA segmentation. Firstly, it is important to create the boundaries between segments. To create it we discuss different methodologies:

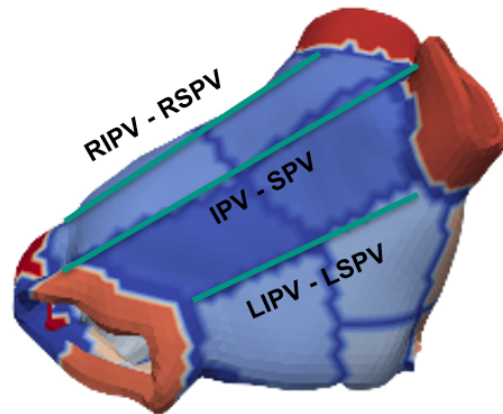


Figure 5.17: Pulmonary veins wall segment boundaries following the geodesic path approach in LA. Three geodesic paths (green) are needed to create the four segments in the wall between pulmonary veins. This geodesic paths are the next: geodesic between RIPV and RSPV, IPV and SPV points, and LIPV and LSPV.

1. Boundaries creation using geodesic paths. Figure 5.12 shows the geodesic path, marked in red, between the RSPV and the left superior pulmonary vein as an example. To create this geodesic path we used the algorithm presented in section 3.2. Basically, the first part is to run the fast marching propagation using a node or several nodes as trigger points (in this example, the RSPV ring is used as trigger points). To create the geodesic from one node to another we need to proceed backward from the desired node until the trigger point. In this example, we wanted to calculate the path between LSPV and RSPV. Because the RSPV ring is used as a trigger, the LSPV is going to be used as end points. So, visiting every neighbor node from LSPV until RSPV we obtained the path with the lower activation time, the geodesic path, between both points (marked in red color).
2. Boundaries creation using artificial geodesic path approach in LA. Figure 5.14 shows the boundary marked in green color that has been created using a geodesic path between two original geodesic paths which were created before (one path from the mid-point of the pulmonary veins to the MV and the other starting from the RIPV to the MV).
3. Figure 5.15 shows segment boundaries following the time activation threshold approach in LA. The boundary marked in green color has been created using a time activation threshold depending on the mid-point between pulmonary veins. This threshold is always fixed to give consistency between geometries.

Using these three different methodologies we were able to create the different segments in the LA. Pulmonary veins segments have been created using the time activation threshold approach. Figure 5.16 shows the creation of pulmonary veins segment boundaries following the time activation threshold approach in the LA. To define the threshold it is necessary

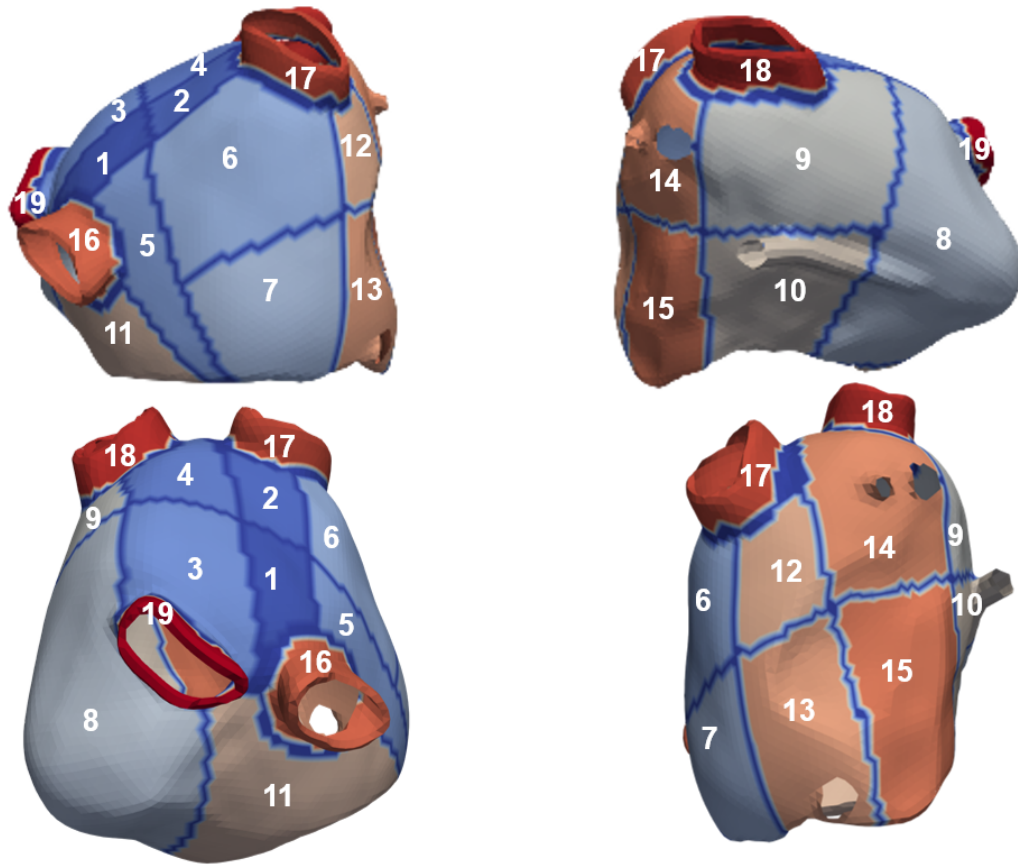


Figure 5.18: Segmentation on the LA consists of 19 segments organized in this way: 4 pulmonary veins segments (LIPV, RIPV, LSPV and RSPV), 4 segments between pulmonary veins, 3 segments on each lateral wall, 4 segments on the anterior wall, next to the septum and 1 segment on the posterior wall, between MV and LIPV-RIPV.

to establish some points which work as triggers. The point number 1 is used to limit the segment boundary between left inferior pulmonary vein (LIPV) and right inferior pulmonary vein (RIPV). The point number 3 is used to limit the segment boundary between LSPV and RSPV. Finally, the point number 2 is used also in both configurations to avoid the penetration of the boundaries in the posterior wall between inferior pulmonary veins and superior.

For example, to create the four segments in the wall between the pulmonary veins, three geodesic paths (green) are needed. These geodesic paths are show in Figure 5.17: geodesic between RIPV and RSPV, IPV and SPV points, and LIPV and LSPV.

Finally, the segmentation on the LA consists of 19 segments (Figure 5.18) organized in this way:

- 4 pulmonary vein segments (LIPV, RIPV, LSPV and RSPV).
- 4 segments between pulmonary veins
- 3 segments on the right lateral wall
- 3 segments on the left lateral wall
- 4 segments on the anterior wall, next to the septum

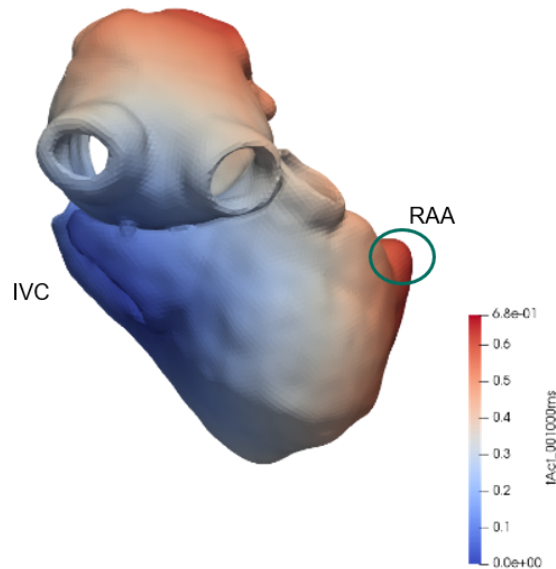


Figure 5.19: Theoretical implementation using fast marching to identify the area of the RA appendage. RAA is defined as the node with the highest activation time starting from the IVC.

- 1 segment on the posterior wall, between MV and LIPV-RIPV.

5.2.2.2 RA segments

AFib is commonly believed to be caused by multiple triggering foci occurring predominantly in the pulmonary veins and, to a lesser extent, in the RA. This is one of the reasons why there is less documentation about RA segmentation compared with LA. Apart from that, geometrically talking the RA is more asymmetrical than the LA. Consequently, the differences between geometries in the RA are more notorious than in the LA and the RA and segmentation is more difficult than the one in the LA. For this reason, we decided to reduce the number of segments in the RA, making them larger compared with the segments in the LA. This approach could be sufficient to avoid the asymmetry between geometries.

Based on our own criteria, a good RA segmentation needs to highlight the more important areas: caval veins and RAA. The creation of the segments which define the caval veins uses the same methodology as the one to create the pulmonary veins, detailed in subsection 5.2.2.1.

Once the caval veins segments are created, it is time to proceed with the RAA segment. One way to define the RAA could be the point with the highest activation time starting the fast marching simulation from the IVC ring (Figure 5.19). The problem with this "theoretical" procedure is that because of the asymmetries on the RA geometries, in more than a half of

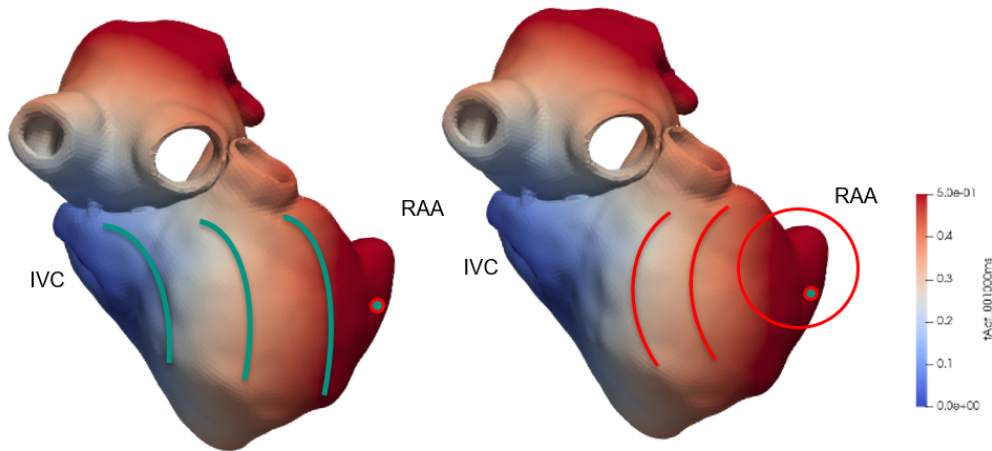


Figure 5.20: Practical implementation using fast marching to identify the area of the RA appendage.

the total cases, the RAA is not well localized with this algorithm. A different approach needs to be used in order to locate the RAA in a correct way.

This practical approach, shown in Figure 5.20 consists in the following steps:

1. Run the theoretical fast marching simulation to find the RAA, starting from the IVC, and save it as $t_{original}$.
2. Find the point with the highest activation time, t_{RAA} .
3. Define an area around it, using a threshold of the highest activation time. The threshold is fixed in all the cases, $threshold = 0.7 \times t_{RAA}$.
4. Run several times the fast marching algorithm, using every time one different node, i , belonging to this area as starting point, until all the nodes are used, t_i .
5. Correlate the original times activation with all the t_i . The goal of correlation between signals, is to find the similarity between them.
6. Finally, find the new point with the highest negative correlation, and define it as RAA.
7. Apply the same threshold to define the new segment around RAA, $threshold = 0.7 \times t_{RAA}$.

Once the RAA is found and the caval veins segments are created, it is time to finish the segmentation of the RA. After that, there were two large spaces which needed the creation of more segments. The anterior wall is divided in two larger segments between the RAA and the caval veins. On the other hand, the posterior wall, is divided into four subsegments between the caval veins and the RAA.

Finally, the RA segmentation is shown in the Figure 5.21. The nine segments are divided in the following way:

- 1 segment defining the IVC.
- 1 segment defining the SVC.

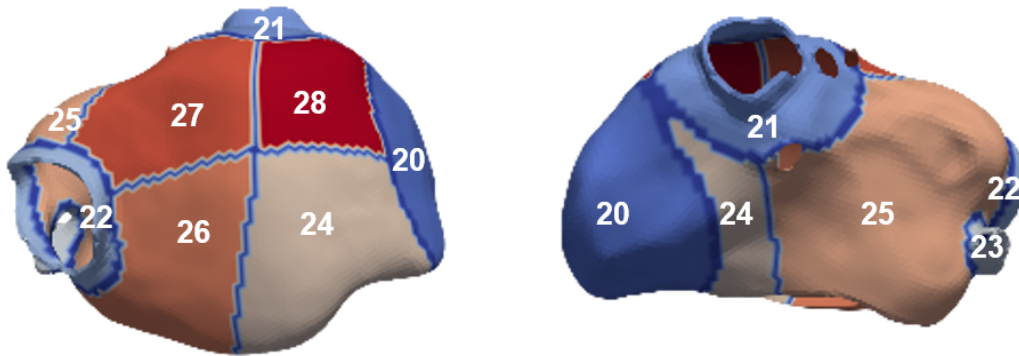


Figure 5.21: RA segments. The left part of this figure shows the segments in the posterior wall. The right part shows the created segments in the anterior wall. All the segments are marked with different colors and numbers.

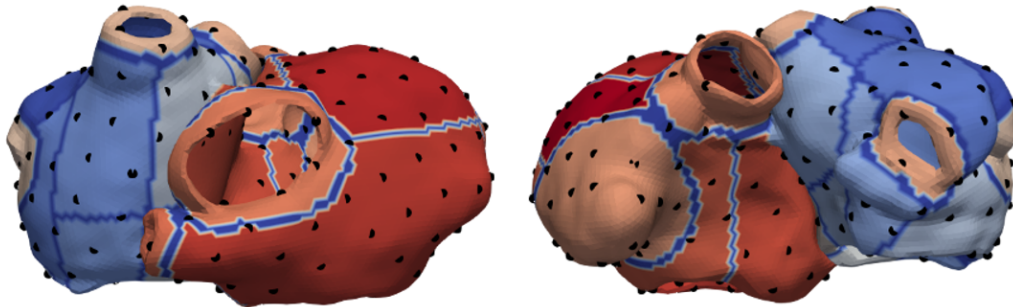


Figure 5.22: Representation of ectopic foci selection in the atria model. Triggers (black points) have been selected using equally separation between them.

- 1 segment defining the cavotricuspid isthmus (CTI).
- 4 segments in the posterior wall of the RA.
- 2 segments in the anterior wall of the RA, one in the septum.

5.3 Excitation simulations

Following this step, a selection of the desired ectopic foci in the atria is needed. Figure 5.22 illustrates the selection of this triggers (black points) in the different segments of the atria, both LA and RA. The ectopic foci have been selected equally distributed by applying Paraview's "clean filter" to merge adjacent points falling below a certain distance threshold. Around 200 ectopic foci have been selected in every atria model.

After fast marching simulations and selecting the ectopic foci, a transmembrane voltage template based on the Couretmanche et al. [21], in which the model was shifted to the time of activation, was used.

5.4 Torso forward calculations

As a result of the standard ECG, factors can affect the signals recorded at the body-surface lead positions and thus induce errors in clinical evaluation. [10] Positional changes of the heart can alter ECG signal amplitude and morphology. Though the heart is anchored at its base by relatively rigid tissue, the apical end of the heart can shift position significantly within the torso due to simple movements of the patient. Even seemingly insignificant movements during such monitoring can result in deviations from the baseline ECG pattern. To propagate the signals from the atria through the torso surface we drove these simulations using the boundary element method presented by Potyagaylo et al. [22]. Cardiac sources were represented by transmembrane voltages on the epicardial and endocardial surfaces bounding the atria.

For forward calculations, an accurate atria-torso model is needed in this thesis. To avoid problems of the positioning of the atria inside the torso, we decided to perform a large number of geometric combinations. This will be explained in the following section.

5.4.1 Atria-torso combinations

Originally we have 8 atria-torso combinations. But, because only 8 configurations are not enough to generalize a NN classifier we decided to expand the number of atria-torso combinations. To avoid this particularization of the solution, 64 atria-torso combinations are presented (8 atria models and 8 torso models give us 64 possible combinations if we mix them).

In the default models, every atria model has its corresponding torso model, meaning that, e.g., the atria model dk01 is perfectly matched with the torso dk01. But what happens if we place this atria model into a different torso? If we place the atria into a different torso, the atria will not end up at the correct location in this torso. They might touch the torso wall or even worse lie outside of the torso model.

To avoid this problem reallocations of the atria are needed in every torso model. The solution is shown in Figure 5.23. The figure on the left shows the corresponding atria (blue-red color) in the torso model. The mid-figure shows what happens if we place a new atria (gray color), which does not belong to this torso, inside this torso model. A wrong placement of the atria occurs here. Finally, aligning the center of mass of both atria (blue-red color) makes it possible to put the new atria in place of the original one. Here, the center of mass was approximated by calculating the mean of all positions in each of the atrial geometries.

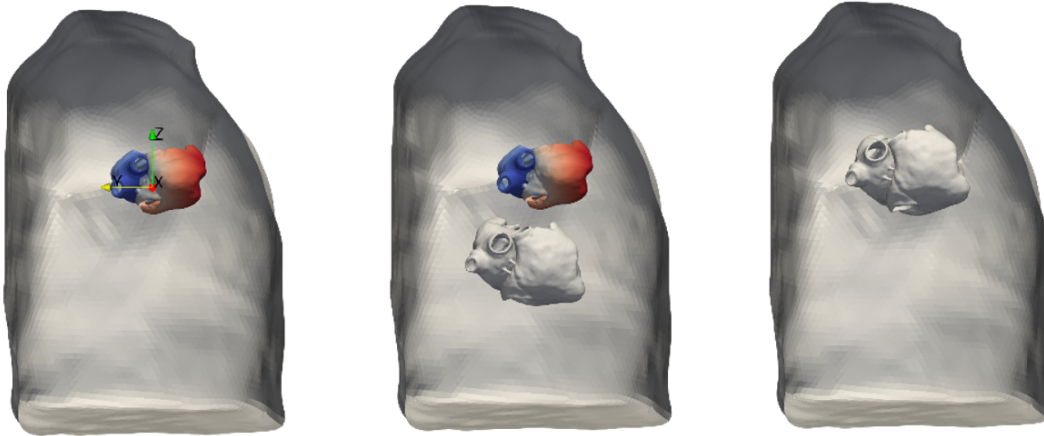


Figure 5.23: Representation of the torso's center of mass calculation for the correct placement of the atria. The figure on the left shows the corresponding atria (blue-red color) in the torso model. The mid-figure shows what happens if we place a new atria (gray color), which does not belong to this torso, inside this torso model. A wrong placement of the atria occurs here. Finally, aligning the center of mass of both atria (blue-red color) makes it possible to put the new atria in place of the original one.

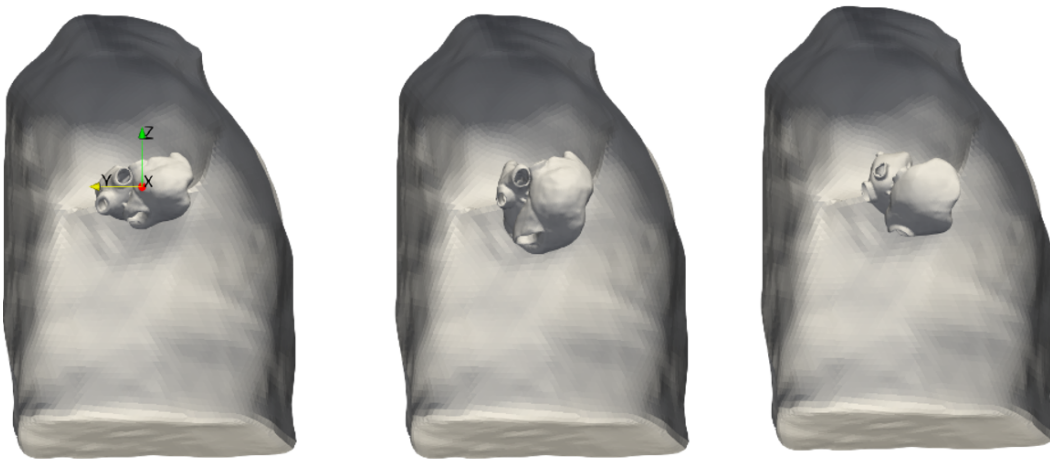


Figure 5.24: Representation of the torso's translation and rotation variations.

Once all the atria are in the correct place of the different torso models, translation and rotation variations are applied. To achieve these variations the torso model is fixed and the atria are displaced within the torso. The methodology to apply these variations is detailed in the following lines:

- For each coordinate axis, calculate 64 equally distributed translations and select one of them for every atria-torso combination. The translations are applied within the following ranges:
 - y-axis: 0...20 *mm*
 - x-axis: -10...10 *mm*
 - z-axis: -10...10 *mm*

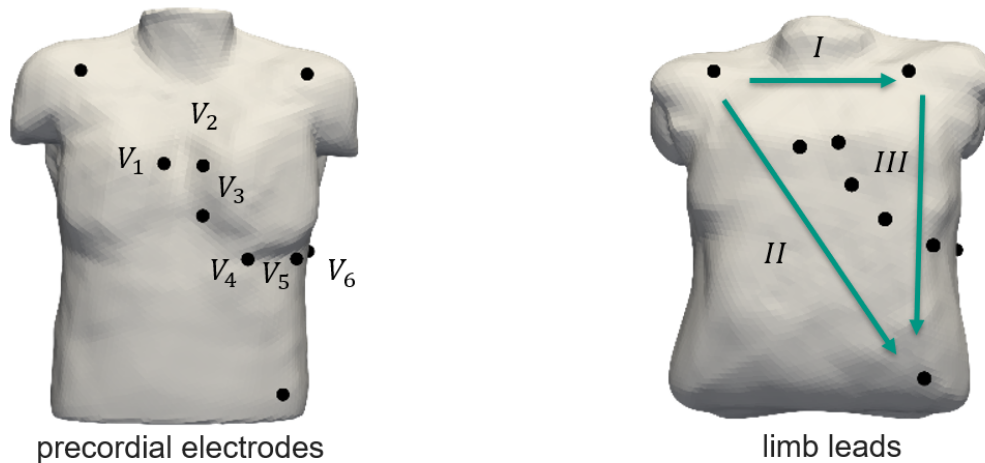


Figure 5.25: Representation of the 12-lead ECG in the torso model.

- For each coordinate axis, calculate 64 equally distributed rotations, and select one of them for every atria-torso combination. The rotations are applied within the following ranges:
 - y-axis: $-10...10^\circ$
 - x-axis: $-10...10^\circ$
 - z-axis: $-10...10^\circ$

5.4.2 12-lead ECG

In this section, we explain the process of obtaining the 12-lead ECG in the torso model. Once the forward calculation is done, ECG electrode locations are needed for the 12-lead ECG. Figure 5.25 illustrates the nine electrodes distribution on the torso around the atria. Calculations shown in chapter 2 transform the electrode potentials into a 12-lead ECG. In Figure 5.25 two parts are differentiated. The left torso shows the precordial electrodes, and the right torso shows the limb leads. Potential differences between the limb electrodes are the basis for the other three standard ECG leads, I, II and III, and the augmented limb leads are explained in chapter 2.

5.5 Feature extraction

The classification of ECG signals requires the generation of features that accurately characterize these patterns in order to enable their type or class differentiation. Features should represent the ECG patterns in such a way that the differences of the morphology of the ECG

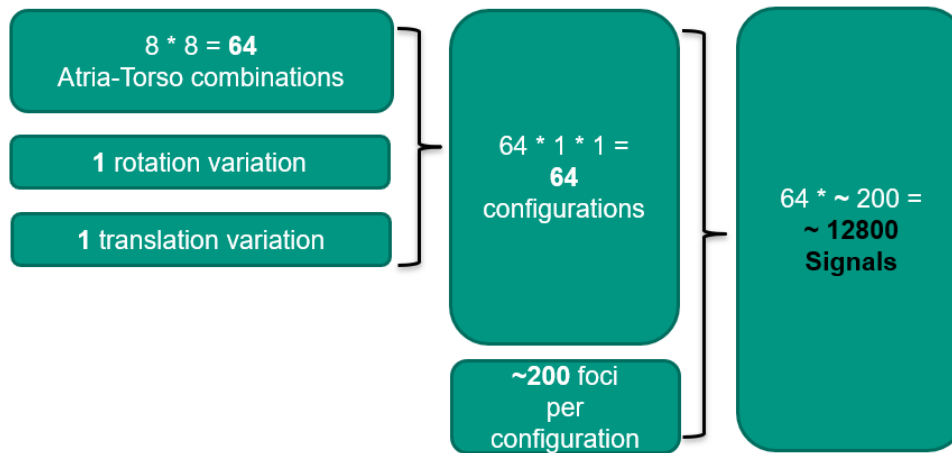


Figure 5.26: Estimation of the number of signals used in the classification.

waveforms are suppressed for the same type of heartbeats, and enhanced for waveforms belonging to different types of beats. This is important, since we observe that different morphologies are expected to mainly change with the type of heartbeat whereas absolute amplitudes are largely dependent on torso conductivity and size. Features should capture morphology in particular and should be normalized for differences in amplitudes. Because of the absence of ventricular response in our atria models, this thesis is focused on the P-wave characteristics. Most existing studies to classify the ectopic foci are only based on P-wave polarity, which has not shown enough accuracy to classify the ectopic foci into atrial segments. [1]

In this thesis, a different feature extraction technique has been applied, primarily focusing on the independent signal extraction (FastICA) and the de-correlation of signals (PCA).

Finally, an estimation of the signal database is represented in Figure 5.26. Simulating around 200 ectopic foci per atria in 64 configurations, yields a database of around 12800 signals. These signals will be used in section 5.5 to extract features. For feature extraction, we assumed that all signals are aligned to the time of excitation onset. In reality, this time is not known and cannot easily be determined from body surface potentials. Results therefore represent a best case scenario. Classification results for a more practicable alignment using the signal's area centroid can be found in the appendix chapter 10.

5.5.1 PCA

Dimensionality reduction using PCA is a useful approach to use on feature extraction. The basis of the PCA algorithm is presented in the section 3.3. Usually, if the percentage of the cumulative sum of eigenvector values is 90%, the transformed vectors will be enough to represent the original vectors. In PCA, the first eigenvector with the largest eigenvalue is the feature with the greatest explanatory ability. Basically, the calculation of the PCA for our database gives us features to train the NN.



Figure 5.27: Synthetic data representation and its decomposition using PCA and FastICA.

5.5.2 FastICA

The FastICA approach aims to calculate maximum statistically independent features. It does not require a pre-whitening step: first, also a dimensionality reduction is performed using PCA. Then, FastICA is applied, performing an eigenvalue decomposition of the data covariance matrix and the data is transformed, so that its covariance matrix is given by an identity matrix.

The main differences between PCA and FastICA are the following:

- PCA removes correlations, but not higher order dependence. On the other hand, FastICA removes correlations and higher order dependence.
- PCA: some components are more important than others (eigenvalues). On FastICA, all components are equally important.
- PCA: vectors are orthogonal. FastICA vectors are not orthogonal. [23]

A useful way of visualizing these differences is shown in Figure 5.27. Here, a synthetic data representation is illustrated. While ICA is used to explain the variance in the data in terms of independent components, PCA is used to explain the variance in terms of uncorrelated, but generally dependent components of decreasing importance. Before testing both procedures in the NN, we thought that FastICA could represent the original data in a better way than PCA. It is more useful for discriminating signals from different foci locations.

The FastICA algorithm is applied in every lead matrix (there are 12 matrices, one per lead). The matrices individually consist of 64 submatrices (one per atria-torso combination). Every atria-torso combination is a $foci \times time$ matrix. Time is represented in the columns (200 ms, 200 time steps of 1 ms) and every ectopic foci is represented in a different row. Figure 5.28 illustrates this procedure. Applying FastICA to every lead matrix defines the independent components for each lead, consisting of 200 time steps.

Representation of the FastICA independent components for multiple ectopic foci in the same lead is illustrated in Figure 5.29. Basically, FastICA independent components are hat

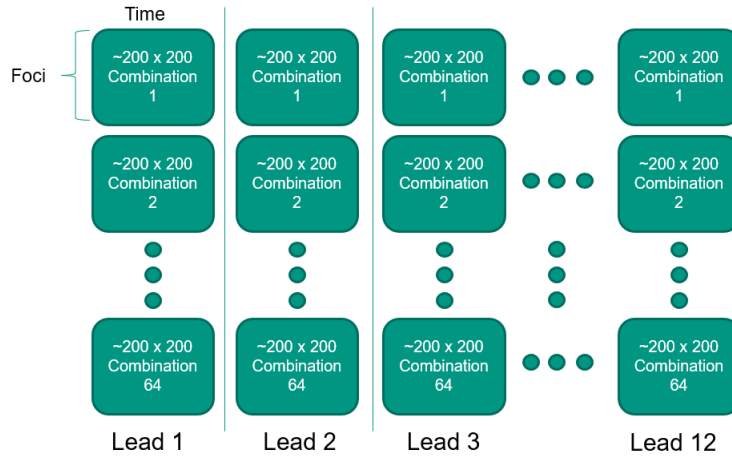


Figure 5.28: Matrix representation of the signals. Every lead has his correspondent matrix. Every matrix is composed of 64 atria-torso combinations. Every combination is a $foci \times time$ submatrix.

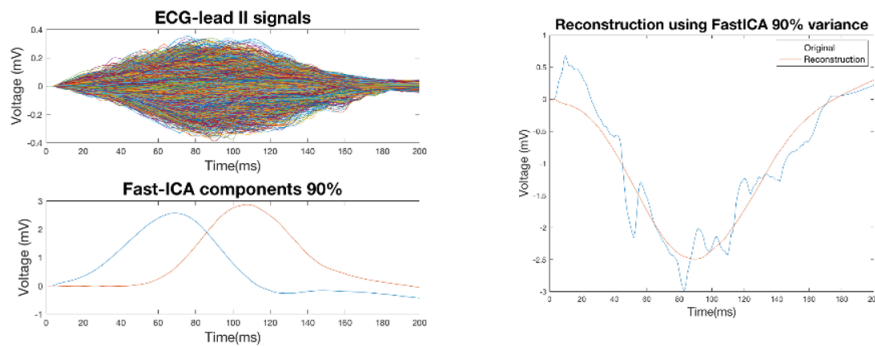


Figure 5.29: Representation of the FastICA independent components with 90% variance applied in multiple ectopic foci in the same lead. Right image represents the original signal and his reconstruction using FastICA.

functions which can be used to reconstruct the original signal using least squares regression. A larger fraction of variance obtained during dimensionality reduction leads to a higher number of independent components. Consequently, a reconstruction with higher frequency features of the original signal is achieved. Figure 5.29, Figure 5.30 and Figure 5.31 show the result of FastICA with different variances, 90%, 95% and 99%,

5.6 Classification

The application of machine learning methods has become an important trend in atrial ectopic foci localization prediction. Many solutions have been proposed for developing automated systems to classify atrial ectopic beats into segments, based on the BSPM using SVM. [6]

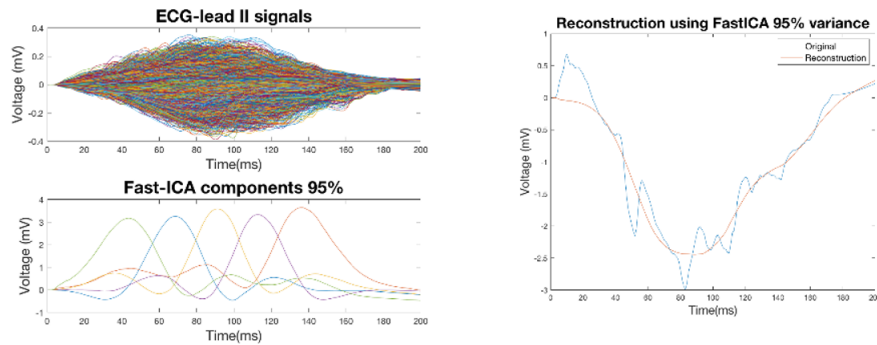


Figure 5.30: Representation of the FastICA independent components with 95% variance applied in multiple ectopic foci in the same lead. Right image represents the original signal and his reconstruction using FastICA.

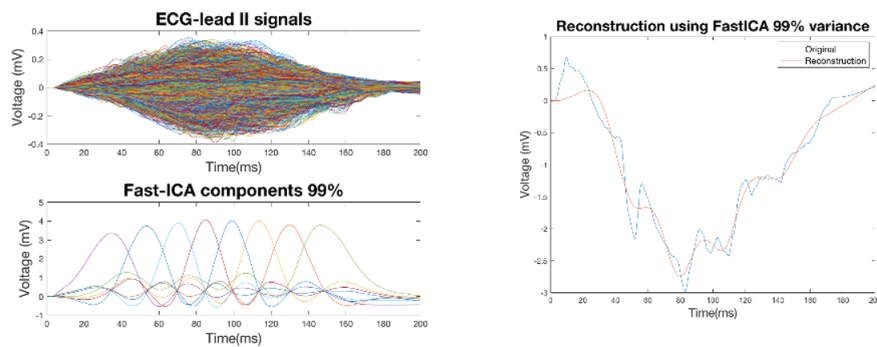


Figure 5.31: Representation of the FastICA independent components with 99% variance applied in multiple ectopic foci in the same lead. Right image represents the original signal and his reconstruction using FastICA.

But they did not show sufficient accuracy to solve the problem.

This thesis follows a different methodology, focusing on the 12-lead ECG and NN. The NN theory is explained in section 3.5. The methodology followed in the construction of NN is the following: a ECG recognition system based on NN classifiers usually builds different models, and then the best one is chosen. In the next sections, we discuss different structures and preprocessing methods to finally choose the NN which best classifies the ectopic foci.

5.6.1 Overfitting

One of the main problems that occur during NN training is overfitting. The error on the training set is small, but using new data increases the error. In conclusion, the network has memorized the training, but it has not learned to generalize to new examples.

One method for improving generalization is to use a network that is just large enough to provide an adequate fit. Unfortunately, it is difficult to know beforehand how large a network should be for a specific application. There is one method for improving generalization: early

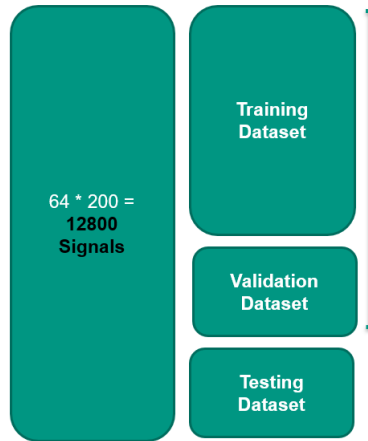


Figure 5.32: Dataset configuration. The different signals are divided into three different groups: training, validation, and testing.

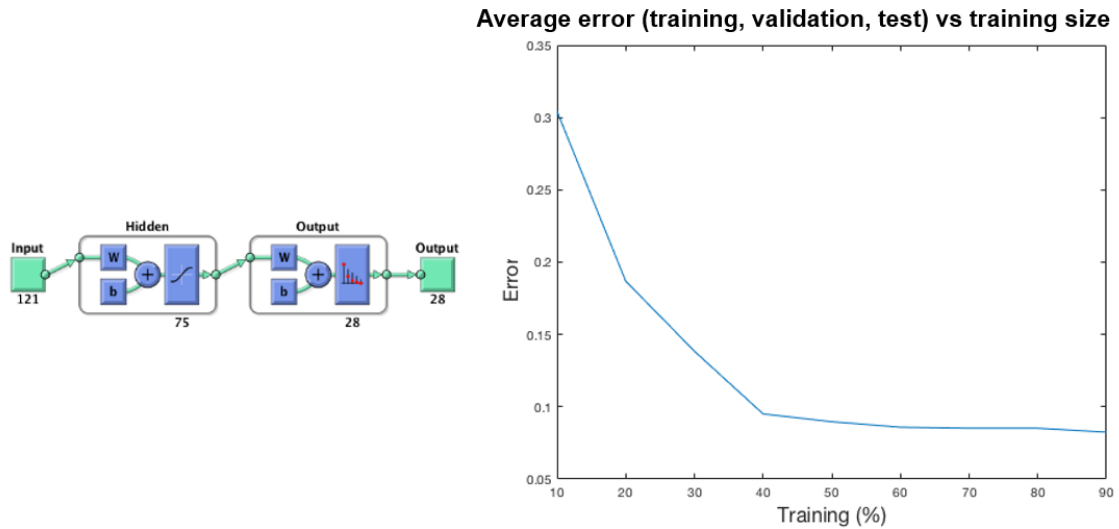


Figure 5.33: Study of the influence of the training proportion in the NN. The figure on the left shows the configuration of the NN, with a 99% variance FastICA and 75 hidden neurons. The right figure shows the average error of the three datasets versus the proportion of training data.

stopping.

In this thesis, we configured all our NN with the early stopping configuration [24]. In this technique, the available data is divided into three subsets (Figure 5.32). The first subset is the training set, which is used for updating the network weights. The second is the validation set, monitored during the training process. When the network begins to overfit the data, the error on the validation set begins to rise. When the validation error increases for a specified number of iterations, the training is stopped, and the weights and biases at the minimum of the validation error are returned. The test set error is not used during training, but it is used to compare different models.

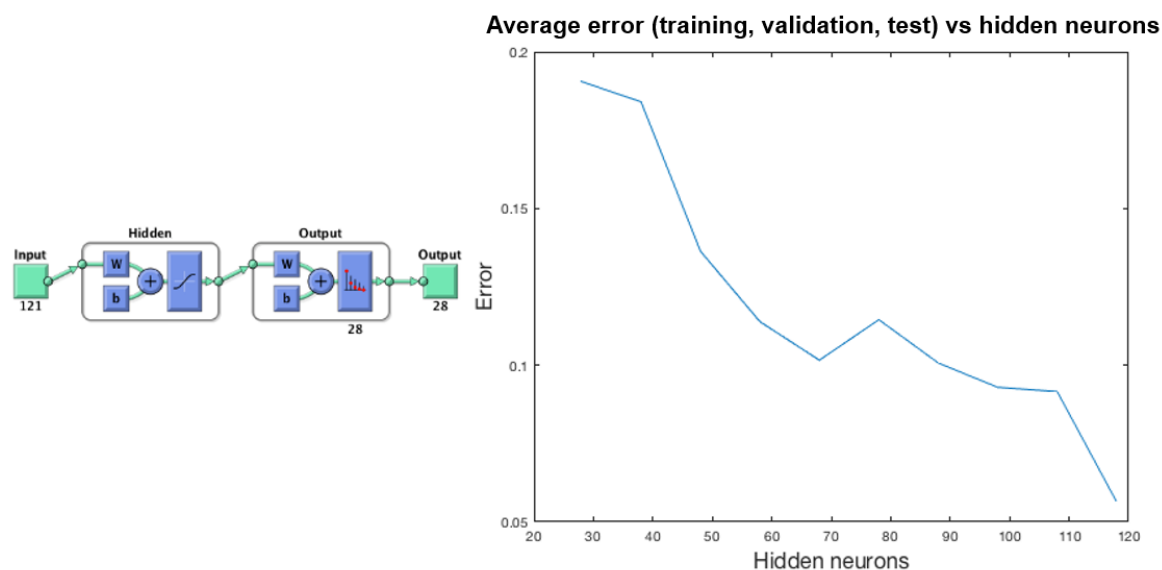


Figure 5.34: Study of the influence of hidden neurons in the NN. The figure on the left shows the configuration of the NN, with a random data division (60% training, 20% validation and 20% testing). The right figure shows the average error of the three datasets versus the number of hidden neurons.

Using the configuration in Figure 5.33, with a 99% variance FastICA and 75 hidden neurons, the average error of the three datasets versus the proportion of training is represented. The remaining percentage that is not used in training, is equally divided between validation and test. In conclusion, a higher percentage used in the training reduced the error in the network, but an excess of them could end in overfitting. The solution is to use a percentage around 60% of the total data as training.

Another important parameter for avoiding overfitting is the number of hidden neurons in the network. The best number of hidden neurons depends on the specific data. There is no fixed rule to choose the number of neurons, but usually is recommended to use a number between the number of input parameters and the number of classes. Increasing the number of hidden neurons increases the number of free parameters and may result in overfitting.

To evade this problem a study of the correct number of hidden neurons is performed. Using the configuration in Figure 5.34, with a random data division (60% training, 20% validation and 20% testing), the average error of the three datasets versus the number of hidden neurons is represented. In conclusion, a higher number of hidden neurons reduced the error in the network, but an excess of them could end in overfitting. The solution is to use a number of neurons between the number of input features and the number of classes. In this case, using a 99% variance FastICA, the number of input features are 121. On the other hand, the number of classes (segments) in the atria model is 28 (19 for LA and 9 for RA). Looking at the representation of average error vs hidden neurons, a compromise between the number of neurons and accuracy is around half of the number of input features.

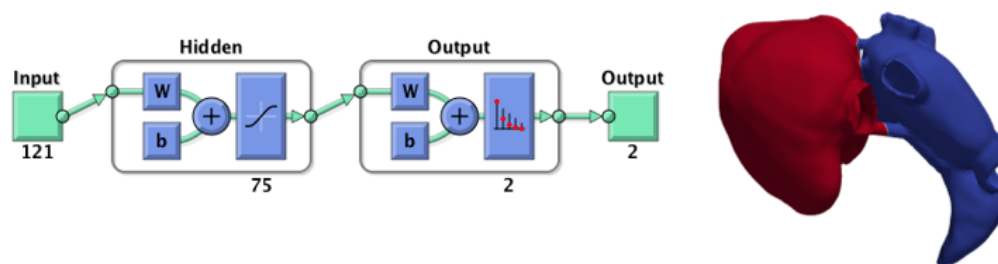


Figure 5.35: Binary NN classification configuration with the purpose of the separation between LA and RA.

5.6.2 Random data division

5.6.2.1 LA and RA classification

Also, an interesting approach could rely on how well the separation between LA and RA could be done with a normal 12-lead ECG. The classifier is created in the way that appears in Figure 5.35. In this case, using a 99% variance FastICA in the ECG data, the number of input features are 121. A random data division is done with 75 hidden neurons in the hidden layer. The output consists of 2 different classes: LA and RA. The results are shown in chapter 7.

5.6.2.2 Multiple segments classification

Once the binary classification between LA and RA is performed, it is time to perform a more complex classification between segments. This type of classification uses early stopping with a random division between training, test and validation sets, meaning that all the 64 atria-torso combinations are used and divided randomly between the three subsets (60% training, 20% validation and 20% testing). In this classification, we used different variances and features (PCA and FastICA). The results of this type of classification are shown in chapter 7.

5.6.3 Atria data division

Figure 5.36 shows the configuration of this classifier. This type of classification differs from the random data division in the way that 7 atria and 8 torso models are used as training and validation subsets, meaning 56 atria-torso combinations. The remaining atria model is combined with the 8 torso models and the data is used as testing subset. In this configuration we used a 99% variance FastICA in the ECG data, the number of input features are 121, and

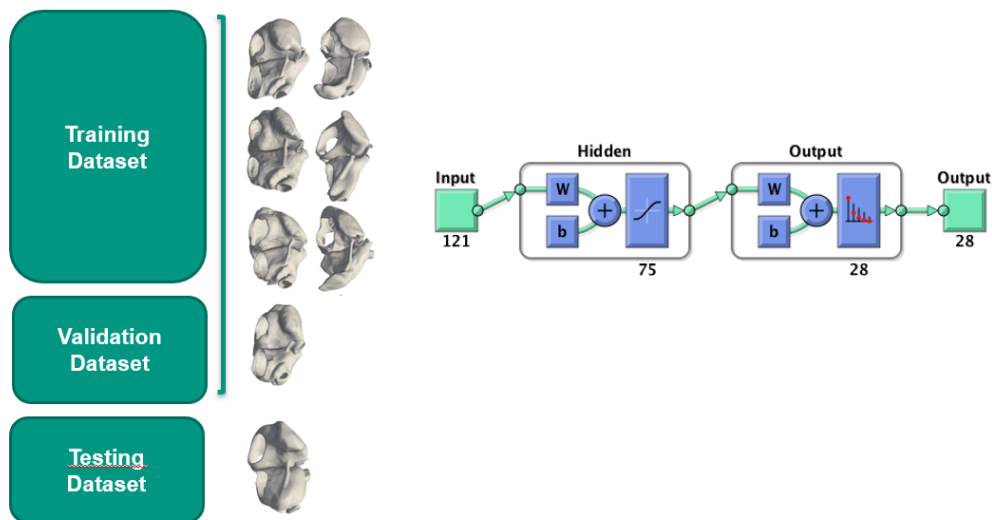


Figure 5.36: NN configuration using atria data division. In this configuration 7 atria models are used as training and validation dataset, keeping one atria model to use as testing.

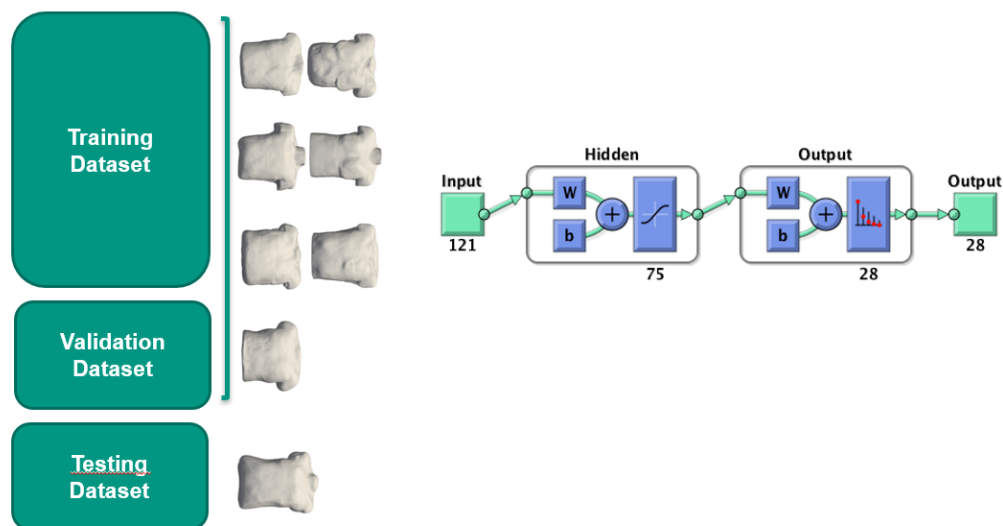


Figure 5.37: NN configuration using torso data division. In this configuration 7 torso models are used as training and validation dataset, keeping one torso model to use as testing.

75 hidden neurons in the hidden layer. The results of this type of classification are shown in chapter 7.

5.6.4 Torso data division

Figure 5.37 shows the configuration of this classifier. This type of classification differs from the random data division in the way that 7 torso and 8 atria models are used as training

and validation subsets, meaning 56 atria-torso combinations. The remaining torso model is combined with the 8 atria models and the data is used as testing subset. In this configuration we used a 99% variance FastICA in the ECG data, the number of input features are 121, and 75 hidden neurons in the hidden layer. The results of this type of classification are shown in chapter 7.

PART III

RESULTS

Atria segmentation results

6.1 Left atrium segmentation results

Using the geodesic based approach, detailed in the subsection 5.2.2, the final LA segments in all the atria models are presented in Figure 6.1 and Figure 6.2.

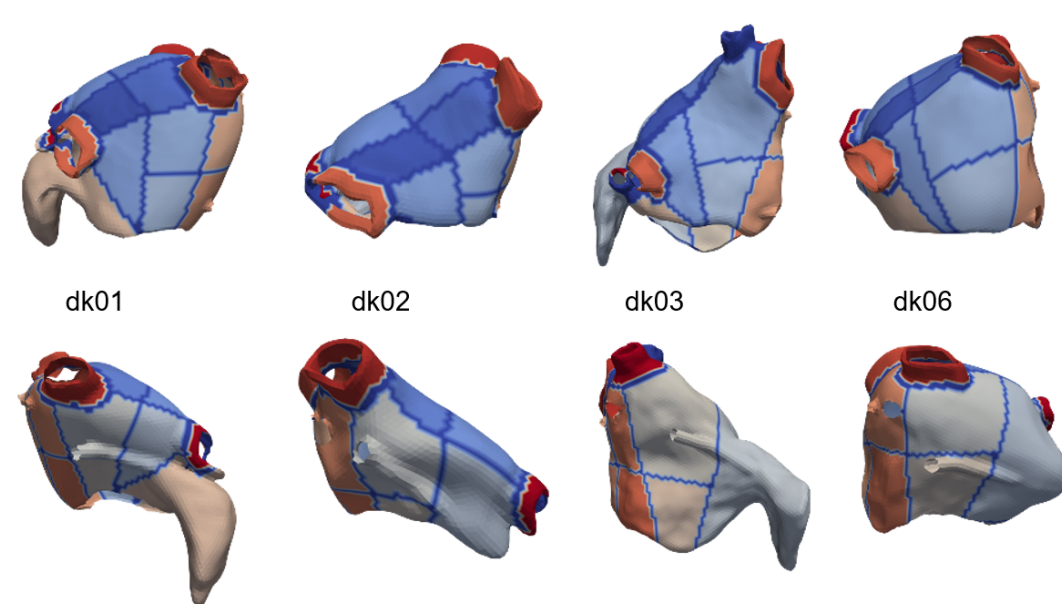


Figure 6.1: LA segmentation of the first 4 atria models. Every segment in the same atria model is denoted with a different color

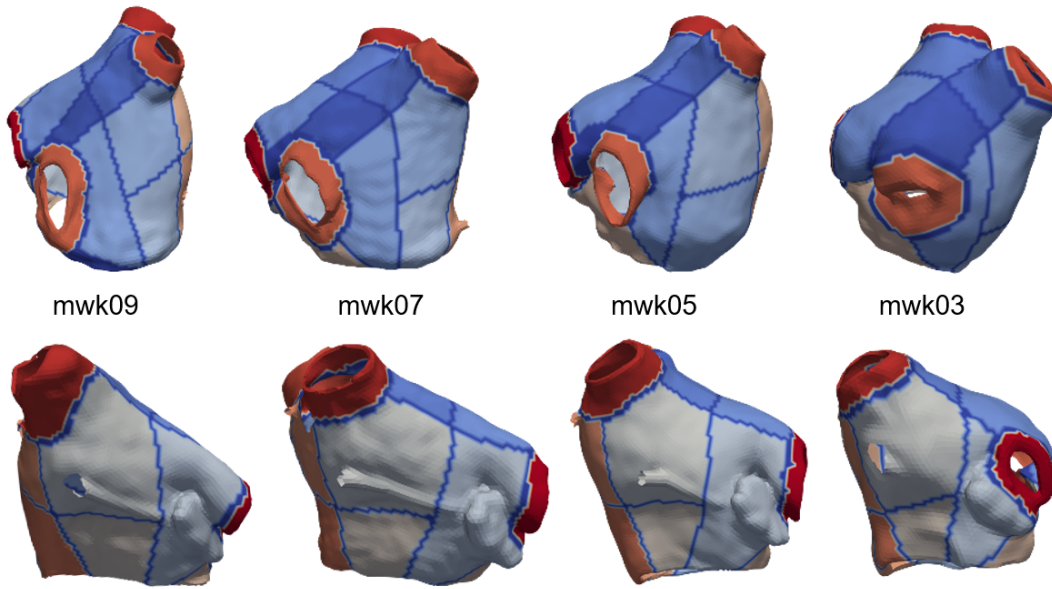


Figure 6.2: LA segmentation of the second 4 atria models. Every segment in the same atria model is denoted with a different color

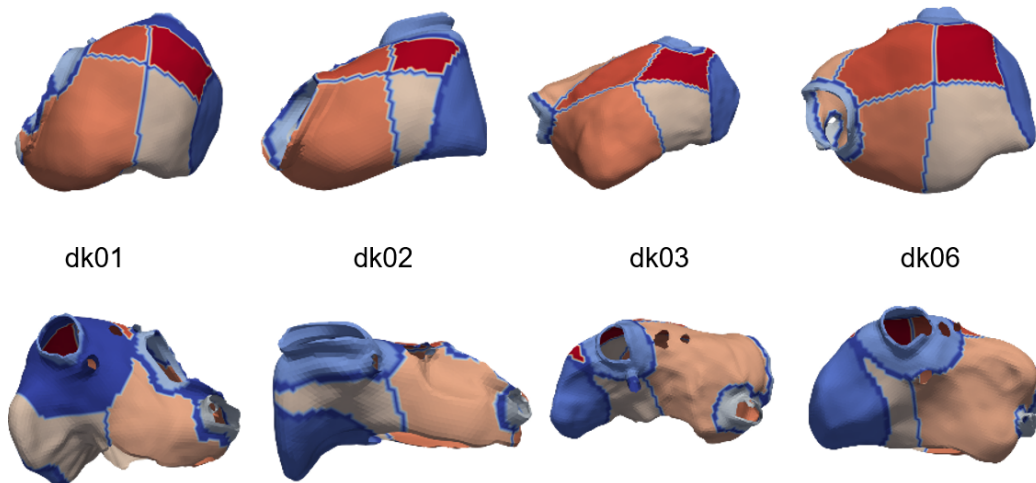


Figure 6.3: RA segmentation of the first 4 atria models. Every segment in the same atria model is denoted with a different color

6.2 Right atrium segmentation results

The RA segmentation of all the atria models are presented in Figure 6.3 and Figure 6.4.

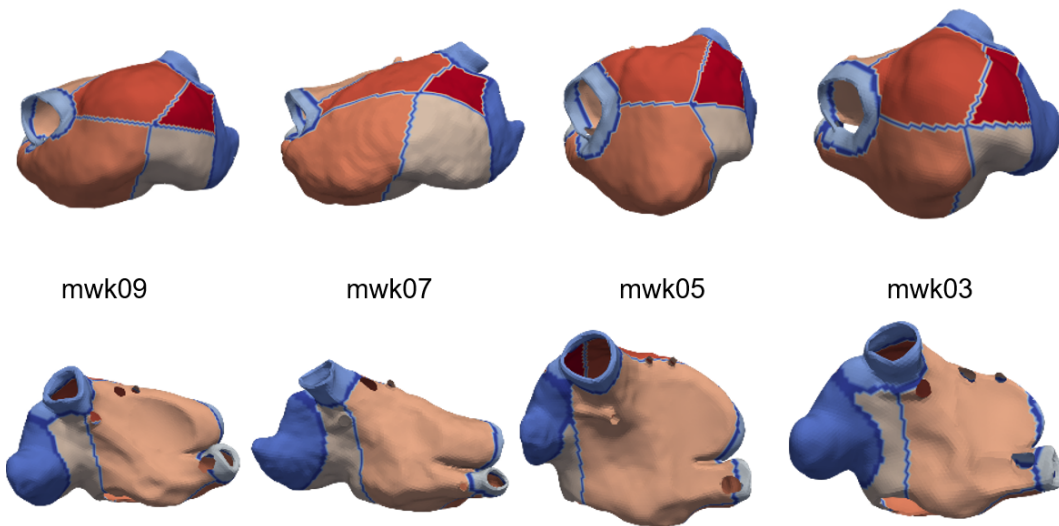


Figure 6.4: RA segmentation of the second 4 atria models. Every segment in the same atria model is denoted with a different color

Classification results

The methodology followed in the construction of NN is detailed in section 5.6. In this chapter several types of metrics are presented:

Condition positives (P) the number of real positive cases in the data.

Condition negatives (N) the number of real negative cases in the data.

True positives (TP) the number of actual positives that are correctly identified.

True negatives (TN) the number of actual negatives that are correctly identified.

False positives (FP) the number of misclassified classes.

False negatives (FN) the number of cases in which a test result improperly indicates no presence of a condition, when in reality it is present.

$$\text{Accuracy } ACC = \frac{TP + TN}{P + N} = \frac{TP + TN}{TP + TN + FP + FN}$$

$$\text{True positive rate } TPR = \frac{TP}{P} = \frac{TP}{TP + FN}$$

$$\text{False positive rate } FPR = \frac{FP}{N} = \frac{FP}{FP + TN} = 1 - TNR$$

$$\text{Positive predictive value } PPV = \frac{TP}{TP + FP}$$

$$\text{False discovery rate } FDR = \frac{FP}{FP + TP} = 1 - PPV$$

Table 7.1: Confusion matrix definition

		True class		Total
		Positive	Negative	
Predictive class	Positive	TPR	FPR	PPV
	Negative	FNR	TNR	FDR
Total		TPR	FPR	ACC

Table 7.2: LA and RA classification confusion matrix

		True class		Total
		LA	RA	
Predictive class	LA	47.5%	0.3%	99.5%
	RA	4.9%	47.4%	90.6%
Total		90.7%	99.5%	94.9%

Confusion matrix A confusion matrix (Table 7.1) is a specific table layout that allows visualization of the performance of an algorithm. Rows represents the instances in a predicted class and columns represents the instances in an actual class.

Receiver operating characteristic curve A receiver operating characteristic curve, i.e. ROC curve, is a graphical plot that illustrates the diagnostic ability of a classifier system when the discrimination threshold is varied. The ROC curve plot the TPR against the FPR at various threshold settings. This threshold is applied to the probability of a signal belonging to a certain class. [25]

7.1 LA and RA classification

The classifier is created in the way that appears in Figure 5.35. The configuration is explained in subsection 5.6.2.1. After training the NN, the results are shown in the Table 7.2. Also, the ROC of this training is shown in Figure 7.1.

The accuracy of this approach is around 95 % for the testing dataset. This result shows the good performance of the binary classifier between LA and RA. Figure 7.2 shows the misclassified ectopic foci for the atrial model dk06. It can be seen that they are located in the septum, the area between LA and RA. We are convinced that the practical implementation of this approach will be useful in hospitals, but it has to be shown that this still works, if one atrial model is left out completely.

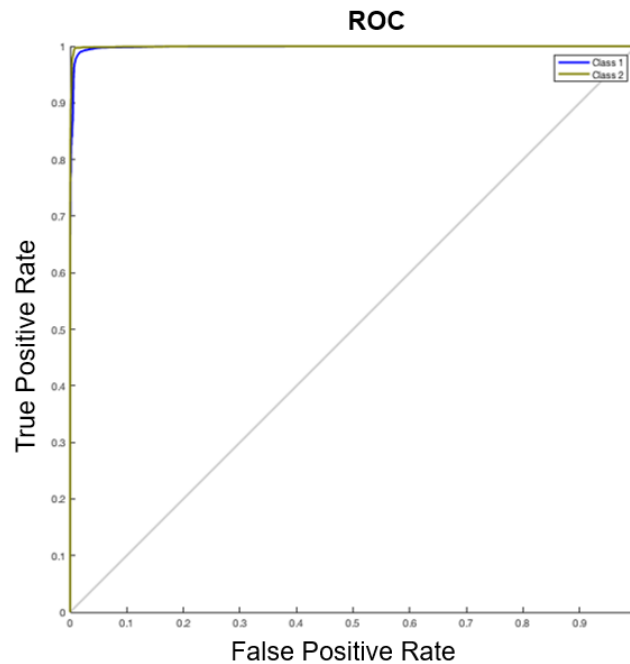


Figure 7.1: Receiver operating characteristic curve of the LA and RA classification. Class 1 corresponds with LA and Class 2 with RA.

7.2 Random data division

In this section, a segment classifier is done with a random data division approach. Different NN configurations and features are used to find the best classifier. The structure of this section is subdivided into two subsections, depending on the features used: PCA or FastICA. Because of the big size of the confusion matrix of 28 segments, we decided not to represent it. Instead of it, a ROC is represented for every configuration.

7.2.1 PCA results

Dimensional reduction using PCA is a useful approach to use on feature extraction. The basis of the PCA algorithm is presented in the section 3.3.

In this section, different classifiers are created using different PCA variances. Figure 7.3, Figure 7.4 and Figure 7.5 show the configuration and ROC of the NN with 90%, 95% and 99%, variance PCA and random data division (60% training, 20% validation and 20% testing).

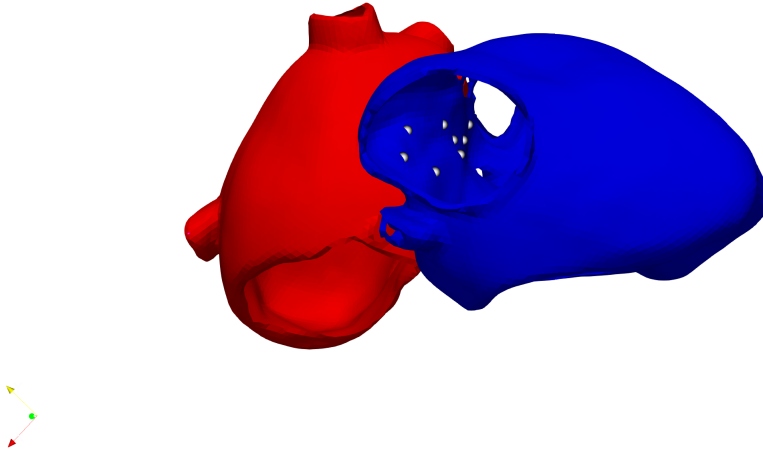


Figure 7.2: Misclassification points (gray) using LA and RA classification. LA is represented in red and RA in blue color.

7.2.2 FastICA results

In this subsection, different FastICA classifiers are created using different variances. Figure 7.6, Figure 7.7, and Figure 7.8 show the configuration and ROC of the FastICA NN with 90%, 95% and 99% variance and random data division (60% training, 20% validation and 20% testing).

7.2.3 PCA vs FastICA results

Here, the results using different features and variances on the NN are presented. To find a good predictor of the accuracy, we trained the NNs several times, to decrease the influence of random initialization, and find the best accuracy value. To represent the results of the different NNs box plots are used. Box plots provide a visualization of summary statistics for sample data and contain the following features:

The tops and bottoms of boxes are the 25th and 75th percentiles. The median is the line in the middle of each box. If the median is not centered, it shows sample skewness.

Figure 7.9 shows the box plot of the different NNs using PCA and FastICA with 90%, 95% and 99% variance. Several conclusions can be extracted from it:

- A higher variance level in the calculation of the principal components (PCA) or independent components (FastICA) results in a higher accuracy. Also, it increases the number of input features.

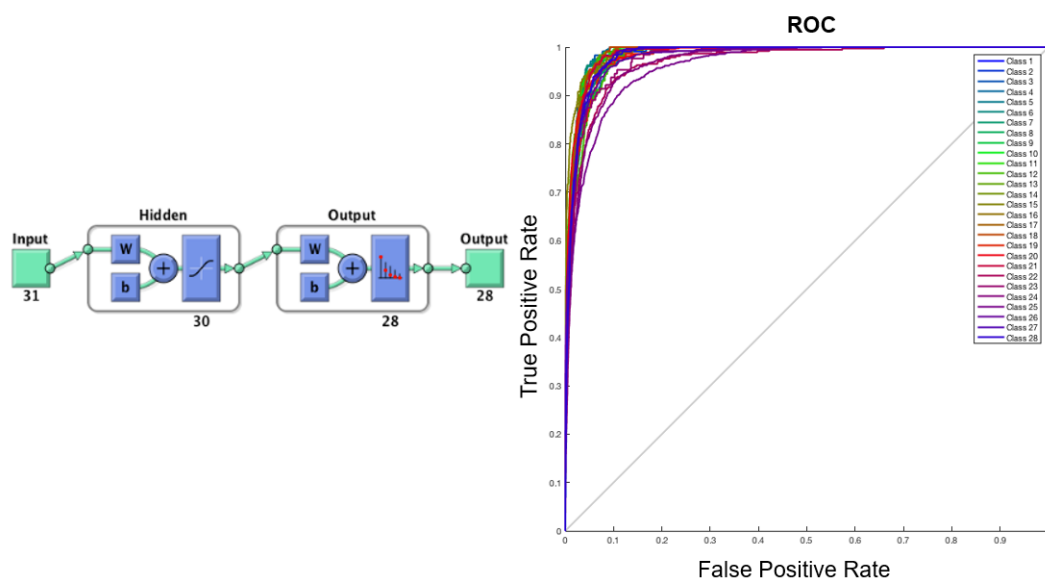


Figure 7.3: NN configuration used with 90% variance PCA and random data division (60% training, 20% validation and 20% testing). In the right part, a ROC of the results is represented. The 28 classes represent the different segments in the atria.

- A higher variance level results in a greater difference between 25th and 75th percentiles. Here the box is bigger compared with the other cases.
- Independent components improve the classification compared with principal components. FastICA achieves better classification than PCA.
- In conclusion, FastICA with 99% variance achieves the best classification, with a median accuracy of around 85%.

NN using FastICA 99% variance Keeping in mind the results from Figure 7.9, we decided to implement our final NN using FastICA 99% variance. The results for every LA segment are shown in Table 7.3 and the results for RA segments are shown in Table 7.4.

Left atrial segments																			
Segments	1	2	3	4	5	6	7	8	9	10	11	12	13	14	15	16	17	18	19
Accuracy	76.7%	79.5%	77.3%	81.5%	82.5%	82.4%	83.2%	87.5%	90.9%	85.0%	90.0%	72.7%	87.5%	79.3%	84.2%	87.0%	89.0%	80.8%	70.1%

Table 7.3: LA segments accuracies using FastICA 99% variance NN.

Right atrial segments									
Segments	20	21	22	23	24	25	26	27	28
Accuracy	92.9%	90.7%	73.1%	74.2%	93.3%	85.6%	91.7%	90.9%	89.2%

Table 7.4: RA segments accuracies using FastICA 99% variance NN.

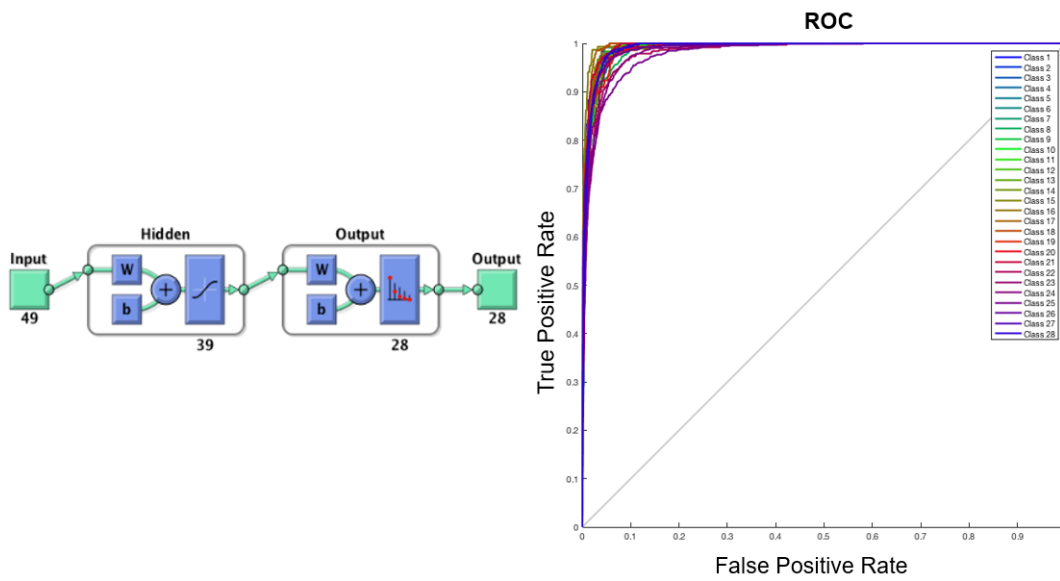


Figure 7.4: NN configuration used with 95% variance PCA and random data division (60% training, 20% validation and 20% testing). In the right part, a ROC of the results is represented. The 28 classes represent the different segments in the atria.

Several conclusions can be drawn:

- The wall between pulmonary veins is the part of LA with the worst classification. This could be because the space between pulmonary veins is not large enough to separate 4 segments. Reducing the number of segments here could improve the classification.

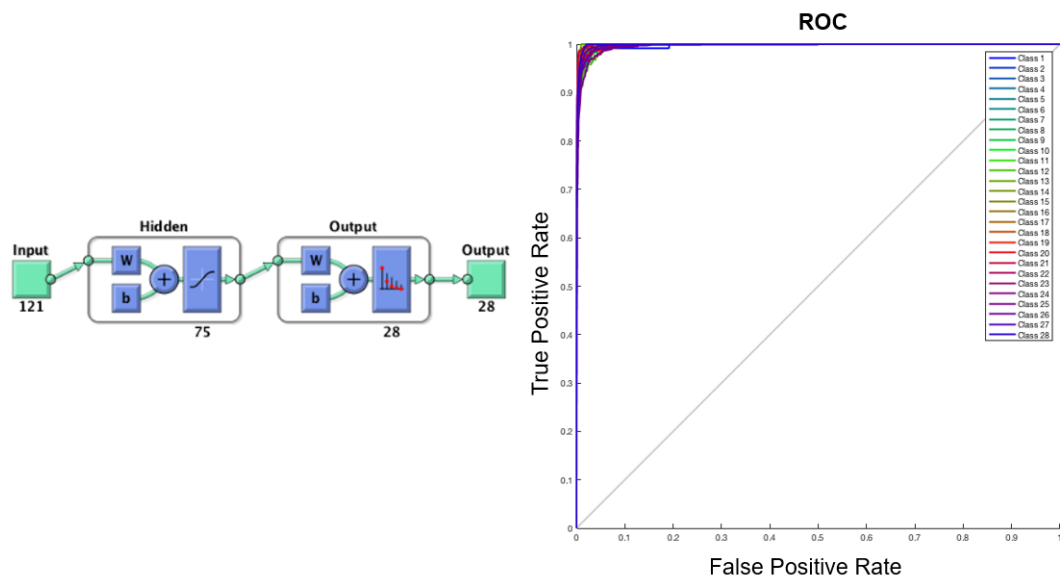


Figure 7.5: NN configuration used with 99% variance PCA and random data division (60% training, 20% validation and 20% testing). In the right part, a ROC of the results is represented. The 28 classes represent the different segments in the atria.

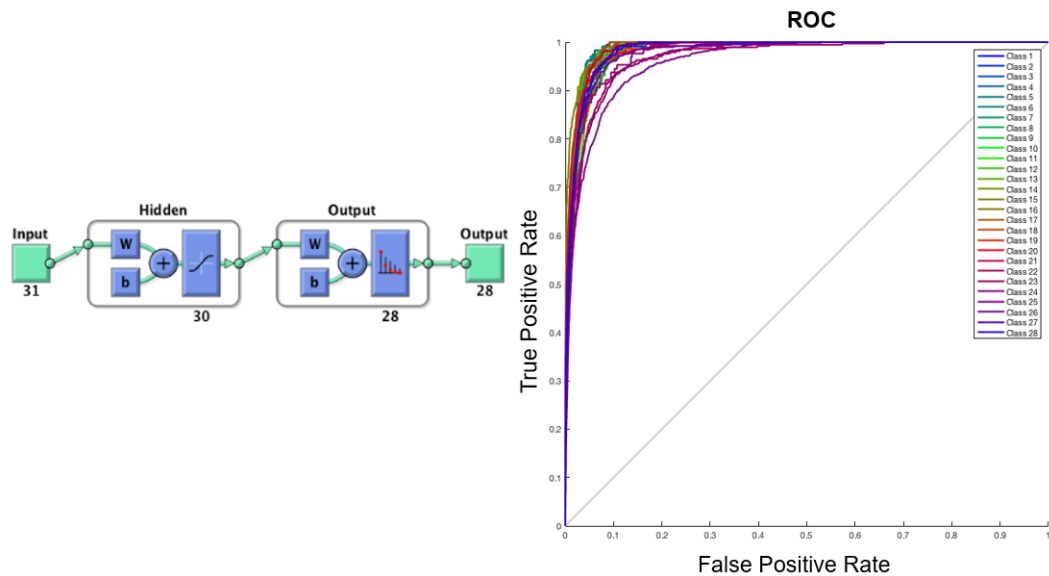


Figure 7.6: NN configuration used with 90% variance FastICA and random data division (60% training, 20% validation and 20% testing). In the right part, a ROC of the results is represented. The 28 classes represent the different segments in the atria.

- Pulmonary veins are difficult to classify because of the size of segments created. Again, a larger segment definition could improve the classification.
- RA and LA appendices are found with high accuracy
- RA segments have better accuracy than segments in the LA. This result can have two reasons: there is a double number of segments in LA than in RA or because the RA is close to the torso surface, thus, more information is contained in the signal.

7.3 Atria data division

Figure 7.10 shows the box plot of the different NNs using atria data division (explained in subsection 5.6.3). In the box plot, the label in the x-axis indicates the atria model that is used as testing.

The main conclusion of this results is that the NN is not able to learn all the atrial geometries with only 8 atria models. Thus, if one atria model is left out during training, the testing results are poor with accuracies around 50%. To solve this problem, we thought that more atria models and variations inside the torso are needed. Once all the possibilities appear in the training, the NN can predict the segment with relatively high accuracy.

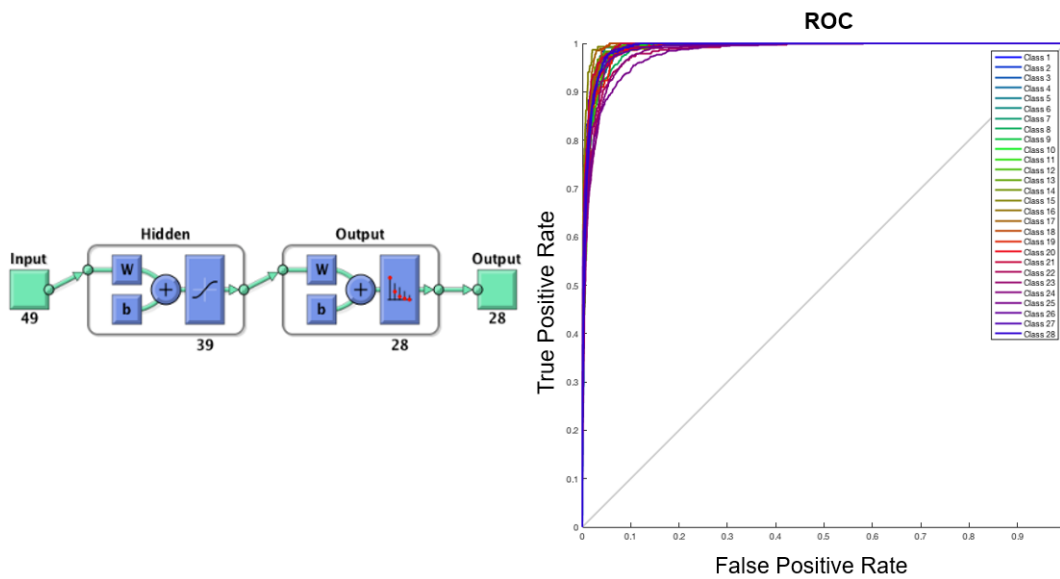


Figure 7.7: NN configuration used with 95% variance FastICA and random data division (60% training, 20% validation and 20% testing). In the right part, a ROC of the results is represented. The 28 classes represent the different segments in the atria.

7.4 Torso data division

Figure 7.11 shows the box plot of the different NNs using torso data division. In the box plot, the label in the x-axis indicates the torso model that is used as testing.

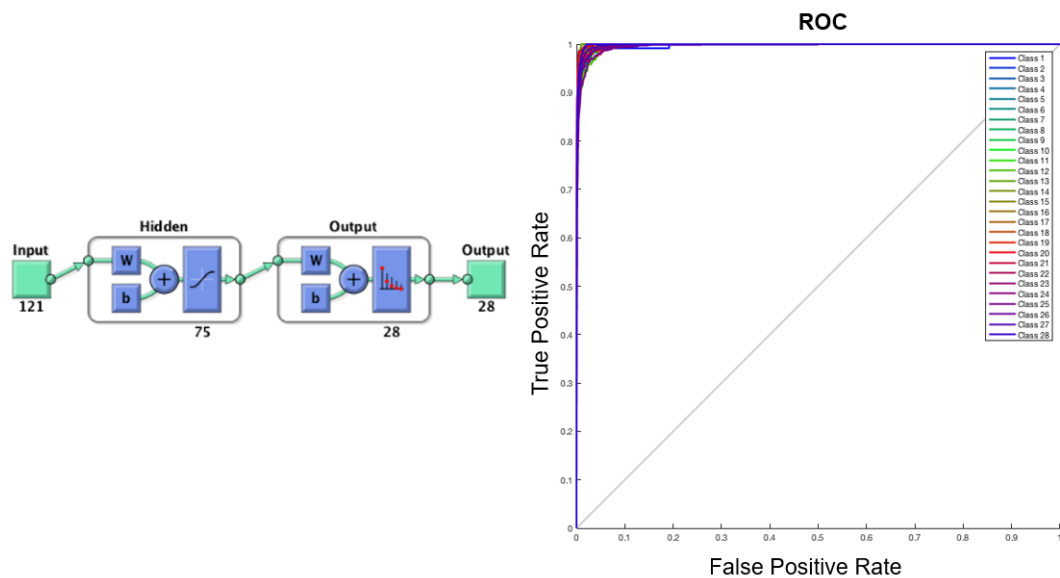


Figure 7.8: NN configuration used with 99% variance FastICA and random data division (60% training, 20% validation and 20% testing). In the right part, a ROC of the results is represented. The 28 classes represent the different segments in the atria.

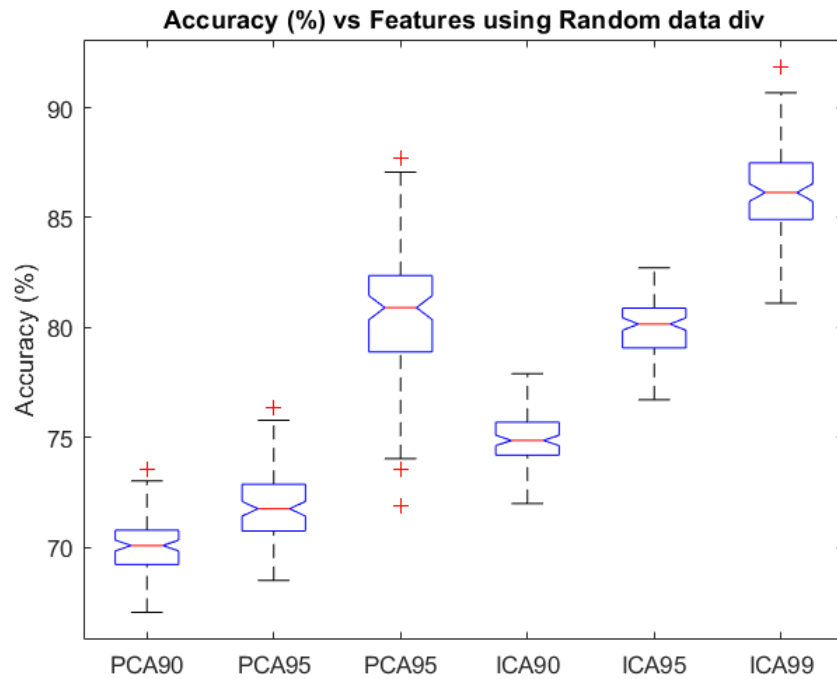


Figure 7.9: Accuracy (%) vs features (PCA and FastICA) boxplot. On each box, the central mark indicates the median, and the bottom and top edges of the box indicate the 25th and 75th percentiles, respectively.

Contrary to the atria data division, here, the signals do not depend on torso too much as atria. The accuracies here are around 80%, like the accuracies in the random data division. The conclusion is that the inclusion of many different torso models is not as important as the inclusion of many different atria models.

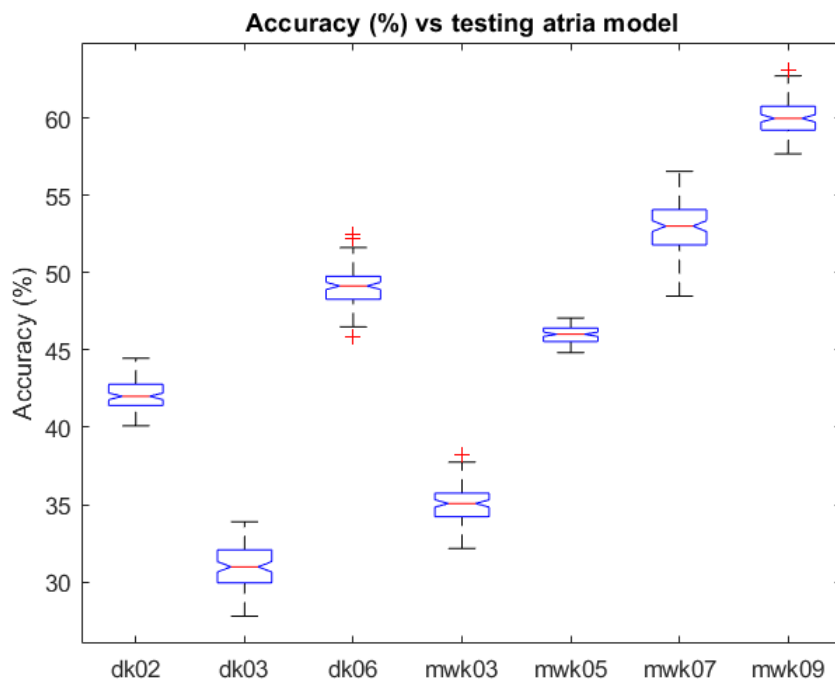


Figure 7.10: Accuracy (%) using atria data division boxplot. The label on the x-axis indicates the atria model that is used as testing. On each box, the central mark indicates the median, and the bottom and top edges of the box indicate the 25th and 75th percentiles, respectively.

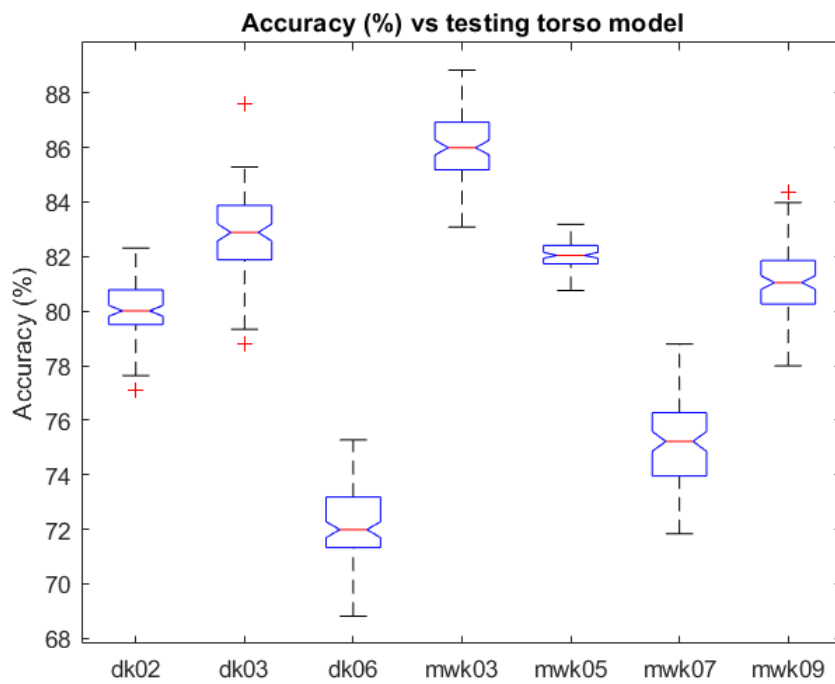


Figure 7.11: Accuracy (%) using torso data division boxplot. The label on the x-axis indicates the torso model that is used as testing. On each box, the central mark indicates the median, and the bottom and top edges of the box indicate the 25th and 75th percentiles, respectively.

Conclusion

In this chapter, conclusions of this thesis are presented. The use of a NN to spatially classify ectopic atrial foci into clearly differentiated geometrically atrial regions, by using the 12-lead ECG has been investigated. Our testing results indicate that ectopic foci with similar 12-lead ECG naturally cluster into differentiated non-intersected atrial regions within one atrial geometry and that new patterns can correctly classified with an approximate accuracy of 85%.

The conclusions are divided into two different aspects: geometrical and classification aspects.

8.1 Geometrical aspects

- Classification depends more on atria than on torso models. To include all possible atria geometries is more important to the ECG than to include all possible torso geometries. For this reason the NN performs better in the torso data division than in the atria data division case.
- Classification performs better in segments with a larger distance to the septum. The LA and RA segments in the septum are very close to each other. For this reason, this part is the most difficult one to classify between LA and RA.
- Ectopic beats in RA and LA are correctly differentiated in most of the cases. The binary classification between LA and RA presents an accuracy higher than 95%. This classifier could be useful in clinical aspects and hospitals.
- Ectopic beats in RA and LA appendices are found with high accuracy. The accuracy for RAA and LAA segments confirms that LAA and RAA are well defined between geometries.
- Ectopic beats in the pulmonary veins and the space between them are the segments with worst classification. Reducing the number of segments while making them larger, could improve the classification.

8.2 Classification aspects

- Classification performs better in larger segments. This affirmation makes sense because if we increase the size of the segments, there is a smaller number of segments to classify and the accuracies are increased. An optimum criteria between segment size and accuracy needs to be found.
- Classification performs better on FastICA features than on PCA. Independent components are more useful for classification than principal components.
- Classification performs better if more principal or independent components are taken into account, leading to more features extracted from the ECG. The accuracy using 99% variance in the signals is higher than using other lower variance level.

Outlook

In this work, an evaluation of the classification of atrial ectopic beats using 12-lead ECG was carried out. A few topics of this work need further research.

The results showed a good accuracy in the classification between segments using 12-lead ECG. Results for random data division are really promising, with an accuracy near 85% using FastICA 99% variance features. The addition of more trigger points in the training stage could lead to a better classification. However, using aligned BSPMs decreases the accuracy to 75% (Chapter 10), which still is a very promising result.

Note also, that LA has worse accuracy than RA. One possible solution could be reducing the number of segments in LA, keeping in mind a compromise between accuracy and precision. However, a model optimization could ignore the undesired behavior for the atria data division NN. An expansion using more anatomical models is crucial for further evaluation of practical results. In atria data division, using a specific atria model, that was not part of the training dataset for testing, deteriorated results. This speaks for a model dependency, and since only eight atria models were used in this work, the results cannot be used in a generalized way. More atria models, rotations and translations are needed to improve the classification using atria data division, and to generalize the classifier for new patients.

Another important point would be the extension of the study featuring an heterogeneous torso model. It should include excitations with anisotropic and varying conduction velocities to increase the similarity between simulated and real signals. This could deliver more realistic ECG signals on the torso, evolving into a real classifier which could be used in clinical procedures.

More or different features could be evaluated in the classification. Analyzing more features in the P-wave could improve the classification. One special case could be the addition of probabilities to the input segments of the NN. The center of the segment would have a probability of 100% to belong to this segment, but the boundaries would have a 50% probability to belong to one segment, and 50% to the neighbor segment. This also, could improve the segment classification.

Although results obtained here are very promising since the application of NNs to simulated data showed good results, the application of the methods to real data is still missing. Since

real ECG data can contain errors or variations in ECG parameters, we can not guarantee a good accuracy in real data. Finally, if neither of this future task improve the classification, more ECG leads or a whole BSPM should be used to improve the ectopic foci classification.

PART IV

APPENDIX

Results for area-aligned ECG signals

In Figure 5.29 we assumed that the time of excitation onset is known precisely, which is not very realistic. To avoid this assumption and test our NN in a more realistic scenario, we aligned the ECG signals in a more practicable and robust way before extracting the features.

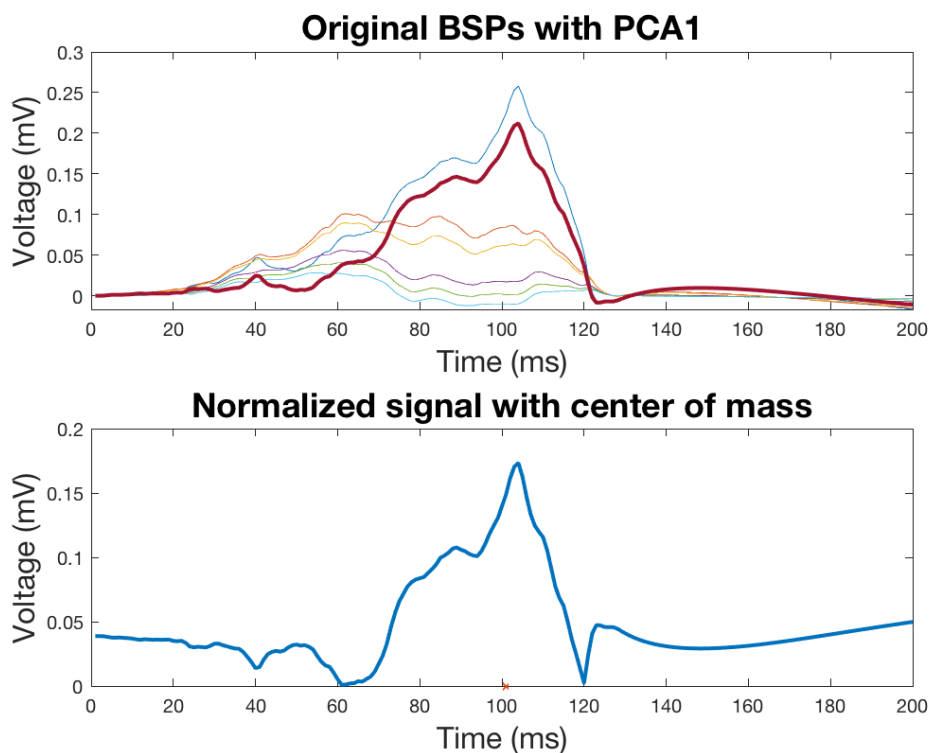


Figure 10.1: Representation of the original BSPMs in one monophasic ectopic foci and his first principal component (bold red curve) along with the normalized signal with the center or mass (red cross).

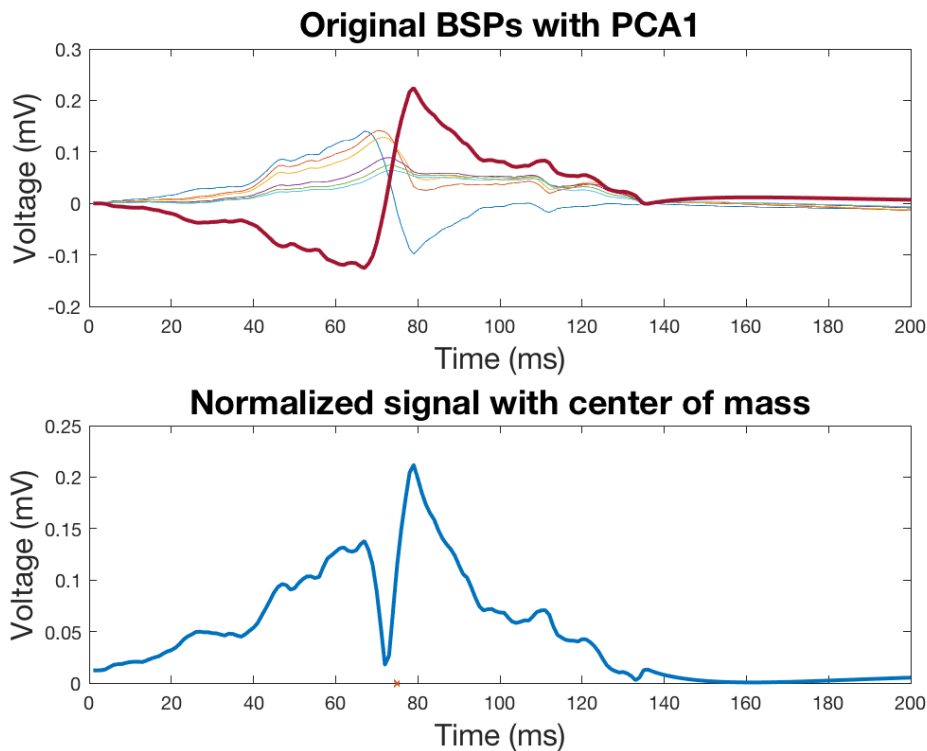


Figure 10.2: Representation of the original BSPMs in one biphasic ectopic foci and his first principal component (bold red curve) along with the normalized signal with the center or mass (red cross).

The alignment of signals is described in the following steps and illustrated in Figure 10.1 and Figure 10.2 for a mono- and biphasic signal, respectively.

- Calculate the first principal component of signals from the six precordial leads (bold red curve).
- Subtract the mean from the first principal component.
- Calculate the absolute value of the resulting signal to prevent errors for biphasic signals.
- Finally, the centroid of the area under the curve is calculated and it is used as central point to align ECG signals of different ectopic foci.

Testing this procedure in the NN with the highest accuracy, random data division and FastICA 99% variance level (Figure 10.3), decreases the classification accuracy about 10% compared to the original alignment using the excitation onset. This result is shown in Figure 10.4.

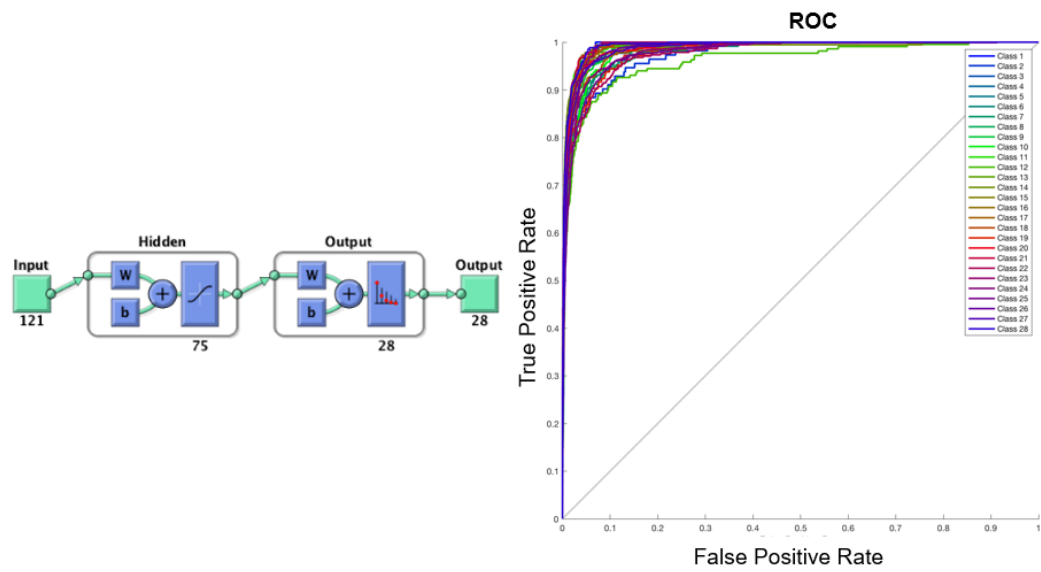


Figure 10.3: NN configuration using area-aligned BSPMs, FastICA 99% variance and random data division.

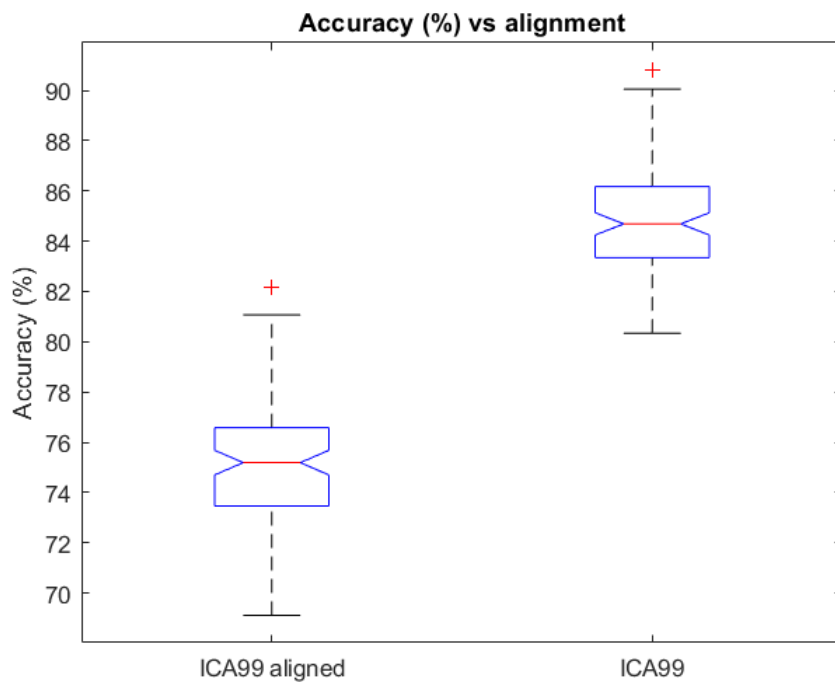


Figure 10.4: Accuracy (%) for an alignment of signals using the area-centroid (left) and the excitation onset (right). On each box, the central mark indicates the median, and the bottom and top edges of the box indicate the 25th and 75th percentiles, respectively.

List of Figures

1.1	Diagram which represents the workflow followed in this thesis.	2
2.1	Illustration of the human heart. Figure inspired by [7].	8
2.2	The six standard chest leads. Figure inspired by [8].	10
2.3	Normal features of the ECG. Figure inspired by [8].	10
3.1	Example architecture of a MLP. Figure inspired by [8].	16
4.1	Models of the eight individual atria used in this thesis.	21
4.2	Models of the eight individual homogeneous torsos used in this thesis.	22
4.3	The influence of discarding different inhomogeneities on some of the lead potentials. Red: results based on the fully inhomogenous (reference) model. Green: discarding lungs, Black: discarding cavities, Magenta: discarding lungs and cavities (homogenous thorax). Figure inspired by [20].	23
5.1	Epicardium and endocardium separation using the atria model. The red color line represents the vein indexes.	26
5.2	Nearest neighbor LA and RA separation approach. LA is marked in blue color and RA is marked in red.	26
5.3	Fast marching trigger point simulation through the atria model. Blue color represents small activation time. On the other hand, the red color represents large activation time.	27
5.4	Tetrahedral mesh LA and RA separation approach. Firstly, the fast marching is running with LA endocardium points as trigger points. Secondly, this time subtract the simulation with RA endocardium points as trigger points. Finally, the application of a zero threshold is able to divide LA (blue) and RA (red) . . .	28
5.5	Tetrahedral mesh LA and RA separation approach. LA is marked in blue color and RA is marked in red.	29
5.6	Approaches to automatically create atrial spatial segments.	29
5.7	Representation of the segments creation challenge. The figure marks the most important veins and locations of the atria.	30
5.8	PCA first component in two different atria models after running several ectopic triggers in the atria. A gradient between LA and RA can be seen.	31

5.9	PCA second component in two different atria models after running several ectopic triggers in the atria. No clear gradient direction can be seen.	31
5.10	PCA third component in two different atria models after running several ectopic triggers in the atria. An anterior-posterior gradient can be seen.	32
5.11	PCA four component in two different atria models after running several ectopic triggers in the atria. An inferior-superior gradient can be seen.	32
5.12	Representation of a geodesic path in the atria. This figure shows the geodesic path between the RSPV and the LSPV marked in red color.	33
5.13	Segment boundaries following the geodesic path approach in the LA. The boundary marked in green color has been created using a geodesic path between LSPV and one fixed point in the MV.	34
5.14	Segment boundaries following the artificial geodesic path approach in the LA. The boundary marked in green color has been created using a geodesic path between two original geodesic paths (one path from the mid-point of the pulmonary veins to the MV and the other starting from the RIPV to the MV).	34
5.15	Segment boundaries following the time activation threshold approach in the LA. The boundary marked in green color has been created using a time activation threshold depending on the mid-point between pulmonary veins. This threshold is always fixed to give consistency between geometries.	35
5.16	Pulmonary veins segment boundaries following the time activation threshold approach in LA. To configure the threshold it is necessary to establish some points which work as triggers. The point number 1 is used to limit the segment boundary between LIPV and RIPV. The point number 3 is used to limit the segment boundary between LSPV and RSPV. Finally, the point number 2 is used also in both configurations to avoid the penetration of the boundaries in the posterior wall between inferior pulmonary veins and superior.	35
5.17	Pulmonary veins wall segment boundaries following the geodesic path approach in LA. Three geodesic paths (green) are needed to create the four segments in the wall between pulmonary veins. This geodesic paths are the next: geodesic between RIPV and RSPV, IPV and SPV points, and LIPV and LSPV.	36
5.18	Segmentation on the LA consists of 19 segments organized in this way: 4 pulmonary veins segments (LIPV, RIPV, LSPV and RSPV), 4 segments between pulmonary veins, 3 segments on each lateral wall, 4 segments on the anterior wall, next to the septum and 1 segment on the posterior wall, between MV and LIPV-RIPV.	37
5.19	Theoretical implementation using fast marching to identify the area of the RA appendage. RAA is defined as the node with the highest activation time starting from the IVC.	38
5.20	Practical implementation using fast marching to identify the area of the RA appendage.	39

5.21	RA segments. The left part of this figure shows the segments in the posterior wall. The right part shows the created segments in the anterior wall. All the segments are marked with different colors and numbers.	40
5.22	Representation of ectopic foci selection in the atria model. Triggers (black points) have been selected using equally separation between them.	40
5.23	Representation of the torso's center of mass calculation for the correct placement of the atria. The figure on the left shows the corresponding atria (blue-red color) in the torso model. The mid-figure shows what happens if we place a new atria (gray color), which does not belong to this torso, inside this torso model. A wrong placement of the atria occurs here. Finally, aligning the center of mass of both atria (blue-red color) makes it possible to put the new atria in place of the original one.	42
5.24	Representation of the torso's translation and rotation variations.	42
5.25	Representation of the 12-lead ECG in the torso model.	43
5.26	Estimation of the number of signals used in the classification.	44
5.27	Synthetic data representation and its decomposition using PCA and FastICA.	45
5.28	Matrix representation of the signals. Every lead has his correspondent matrix. Every matrix is composed of 64 atria-torso combinations. Every combination is a <i>foci</i> \times <i>time</i> submatrix.	46
5.29	Representation of the FastICA independent components with 90% variance applied in multiple ectopic foci in the same lead. Right image represents the original signal and his reconstruction using FastICA.	46
5.30	Representation of the FastICA independent components with 95% variance applied in multiple ectopic foci in the same lead. Right image represents the original signal and his reconstruction using FastICA.	47
5.31	Representation of the FastICA independent components with 99% variance applied in multiple ectopic foci in the same lead. Right image represents the original signal and his reconstruction using FastICA.	47
5.32	Dataset configuration. The different signals are divided into three different groups: training, validation, and testing.	48
5.33	Study of the influence of the training proportion in the NN. The figure on the left shows the configuration of the NN, with a 99% variance FastICA and 75 hidden neurons. The right figure shows the average error of the three datasets versus the proportion of training data.	48
5.34	Study of the influence of hidden neurons in the NN. The figure on the left shows the configuration of the NN, with a random data division (60% training, 20% validation and 20% testing). The right figure shows the average error of the three datasets versus the number of hidden neurons.	49
5.35	Binary NN classification configuration with the purpose of the separation between LA and RA.	50

5.36	NN configuration using atria data division. In this configuration 7 atria models are used as training and validation dataset, keeping one atria model to use as testing.	51
5.37	NN configuration using torso data division. In this configuration 7 torso models are used as training and validation dataset, keeping one torso model to use as testing.	51
6.1	LA segmentation of the first 4 atria models. Every segment in the same atria model is denoted with a different color	55
6.2	LA segmentation of the second 4 atria models. Every segment in the same atria model is denoted with a different color	56
6.3	RA segmentation of the first 4 atria models. Every segment in the same atria model is denoted with a different color	56
6.4	RA segmentation of the second 4 atria models. Every segment in the same atria model is denoted with a different color	57
7.1	Receiver operating characteristic curve of the LA and RA classification. Class 1 corresponds with LA and Class 2 with RA.	61
7.2	Misclassification points (gray) using LA and RA classification. LA is represented in red and RA in blue color.	62
7.3	NN configuration used with 90% variance PCA and random data division (60% training, 20% validation and 20% testing). In the right part, a ROC of the results is represented. The 28 classes represent the different segments in the atria. . . .	63
7.4	NN configuration used with 95% variance PCA and random data division (60% training, 20% validation and 20% testing). In the right part, a ROC of the results is represented. The 28 classes represent the different segments in the atria. . . .	64
7.5	NN configuration used with 99% variance PCA and random data division (60% training, 20% validation and 20% testing). In the right part, a ROC of the results is represented. The 28 classes represent the different segments in the atria. . . .	64
7.6	NN configuration used with 90% variance FastICA and random data division (60% training, 20% validation and 20% testing). In the right part, a ROC of the results is represented. The 28 classes represent the different segments in the atria. . . .	65
7.7	NN configuration used with 95% variance FastICA and random data division (60% training, 20% validation and 20% testing). In the right part, a ROC of the results is represented. The 28 classes represent the different segments in the atria. . . .	66
7.8	NN configuration used with 99% variance FastICA and random data division (60% training, 20% validation and 20% testing). In the right part, a ROC of the results is represented. The 28 classes represent the different segments in the atria. . . .	66
7.9	Accuracy (%) vs features (PCA and FastICA) boxplot. On each box, the central mark indicates the median, and the bottom and top edges of the box indicate the 25th and 75th percentiles, respectively.	67

7.10	Accuracy (%) using atria data division boxplot. The label on the x-axis indicates the atria model that is used as testing. On each box, the central mark indicates the median, and the bottom and top edges of the box indicate the 25th and 75th percentiles, respectively.	68
7.11	Accuracy (%) using torso data division boxplot. The label on the x-axis indicates the torso model that is used as testing. On each box, the central mark indicates the median, and the bottom and top edges of the box indicate the 25th and 75th percentiles, respectively.	69
10.1	Representation of the original BSPMs in one monophasic ectopic foci and his first principal component (bold red curve) along with the normalized signal with the center or mass (red cross).	77
10.2	Representation of the original BSPMs in one biphasic ectopic foci and his first principal component (bold red curve) along with the normalized signal with the center or mass (red cross).	78
10.3	NN configuration using area-aligned BSPMs, FastICA 99% variance and random data division.	79
10.4	Accuracy (%) for an alignment of signals using the area-centroid (left) and the excitation onset (right). On each box, the central mark indicates the median, and the bottom and top edges of the box indicate the 25th and 75th percentiles, respectively.	79

List of Tables

4.1	Influence of the conductivity values in different model compartments, documented by the resulting relative difference (64 leads) between the simulated signals and the reference (fully inhomogeneous model). Table inspired by [20] .	23
7.1	Confusion matrix definition	60
7.2	LA and RA classification confusion matrix	60
7.3	LA segments accuracies using FastICA 99% variance NN.	63
7.4	RA segments accuracies using FastICA 99% variance NN.	63

References

- [1] A. Ferrer-Albero, E. J. Godoy, M. Lozano, et al., “Non-invasive localization of atrial ectopic beats by using simulated body surface p-wave integral maps.” *PloS one*, vol. 12, no. 7, p. e0181263, 1 2017.
- [2] B. Harris, J. A. Shaver, S. W. Gray, et al., “Left atrial rhythm. experimental production in man.” *Circulation*, vol. 37 6, pp. 1000–14, 1968.
- [3] S. Kawano, M. Hiraoka, M. Yamamoto, et al., “Body surface maps of ectopic p waves originating in the left atrium in the dog.” *Journal of electrocardiology*, vol. 22 1, pp. 27–43, 1989.
- [4] D. Giacomelli, J. P. Bourke, A. Murray, et al., “Spatial pattern of p waves in paroxysmal atrial fibrillation patients in sinus rhythm and controls.” *Pacing and clinical electrophysiology : PACE*, vol. 35 7, pp. 819–26, 2012.
- [5] M. A. Colman, O. V. Aslanidi, J. Stott, et al., “Correlation between p-wave morphology and origin of atrial focal tachycardia—insights from realistic models of the human atria and torso,” *IEEE Transactions on Biomedical Engineering*, vol. 58, pp. 2952–2955, 2011.
- [6] C. Reich, T. Oesterlein, M. Rottmann, et al., “Classification of cardiac excitation patterns during atrial fibrillation,” in *Current Directions in Biomedical Engineering*, B. 2016, Ed., vol. 2, no. 1. De Gruyter, 1 2016, pp. 161–166.
- [7] S. Schuler, “Developing and coupling a lumped parameter model of the closed loop human vascular system to a model of cardiac mechanics,” PhD thesis, Karlsruhe Institute of Technology, 2016.
- [8] G. D. Clifford, F. Azuaje, and P. McSharry, *Advanced methods and tools for ecg data analysis*. Norwood, MA, USA: Artech House, Inc., 2006.
- [9] J. A. Sethian and A. Vladimirov, “Fast methods for the eikonal and related hamilton– jacobi equations on unstructured meshes,” *Proceedings of the National Academy of Sciences*, vol. 97, no. 11, pp. 5699–5703, 2000.
- [10] A. Loewe, “Modeling human atrial patho-electrophysiology from ion channels to ecg - substrates, pharmacology, vulnerability, and p-waves,” PhD thesis, Karlsruhe Institute of Technology, 2016.
- [11] Wikipedia, “Geodäte — wikipedia, die freie enzyklopädie,” 2018, [Online; Stand 2. September 2018].
- [12] G. Peyré, M. Péchaud, R. Keriven, et al., “Geodesic methods in computer vision and graphics,” *Foundations and Trends® in Computer Graphics and Vision*, vol. 5, no. 3–4, pp. 197–397, 2010.
- [13] G. H. Dunteman, *Principal component analysis*. Sage, 1989.
- [14] Wikipedia contributors, “Principal component analysis — Wikipedia, the free encyclopedia,” 2018, [Online; accessed 2-September-2018].

- [15] A. Hyvärinen and E. Oja, “Independent component analysis: algorithms and applications,” *Neural networks : the official journal of the International Neural Network Society*, vol. 13 4-5, pp. 411–30, 2000.
- [16] Wikipedia contributors, “Fastica — Wikipedia, the free encyclopedia,” 2018, [Online; accessed 2-September-2018].
- [17] O. Dössel, M. W. Krüger, F. M. Weber, et al., “A framework for personalization of computational models of the human atria,” *2011 Annual International Conference of the IEEE Engineering in Medicine and Biology Society*, pp. 4324–4328, 2011.
- [18] D. M. Harrild and C. Henriquez, “A computer model of normal conduction in the human atria,” *Circulation research*, vol. 87 7, pp. E25–36, 2000.
- [19] M. W. Krüger, G. Seemann, K. S. Rhode, et al., “Personalization of atrial anatomy and electrophysiology as a basis for clinical modeling of radio-frequency ablation of atrial fibrillation,” *IEEE Transactions on Medical Imaging*, vol. 32, pp. 73–84, 2013.
- [20] P. van Dam and A. van Oosterom, “Volume conductor effects involved in the genesis of the p wave,” *Europace : European pacing, arrhythmias, and cardiac electrophysiology : journal of the working groups on cardiac pacing, arrhythmias, and cardiac cellular electrophysiology of the European Society of Cardiology*, vol. 7 Suppl 2, pp. 30–8, 2005.
- [21] M. Courtemanche, R. J. Ramirez, and S. Nattel, “Ionic mechanisms underlying human atrial action potential properties: insights from a mathematical model,” *American journal of physiology. Heart and circulatory physiology*, vol. 275 1, pp. H301–H321, 1998.
- [22] D. Potyagaylo, “Non-invasive electrocardiographic imaging of ventricular activities: Data-driven and model-based approaches,” PhD thesis, 1 2016.
- [23] M. Ivanov, “Comparison of pca with ica from data distribution perspective,” *CoRR*, vol. abs/1709.10222, 2017.
- [24] MATLAB, “Improve neural network generalization and avoid overfitting,” <https://es.mathworks.com/help/nnet/ug/improve-neural-network-generalization-and-avoid-overfitting.html#bss4gz0-32>, 2018 (accessed September 1, 2018).
- [25] W. contributors, “Receiver operating characteristic,” https://en.wikipedia.org/wiki/Receiver_operating_characteristic.